Chemical and physical characterization of the isolated protostellar source CB68: FAUST IV

Imai, M.; Oya, Y.; Svoboda, B.; Liu, H.B.; Lefloch, B.; Viti, S.; ... ; Yamamoto, S.

The Astrophysical Journal, 934:70 (18pp), 2022 July 20 https://doi.org/10.3847/1538-4357/ac77e7

Chemical and Physical Characterization of the Isolated Protostellar Source CB68: FAUST IV

Muneaki Imai[1], Yoko Oya[1,2], Brian Svoboda[3,41], Hauyu Baobab Liu[4], Bertrand Lefloch[5], Serena Viti[6], Yichen Zhang[7], Cecilia Ceccarelli[5], Claudio Codella[5,8], Claire J. Chandler[3], Nami Sakai[7], Yuri Aikawa[9], Felipe O. Alves[10], Nadia Balucani[11], Eleonora Bianchi[5], Mathilde Bouvier[5], Gemma Busquet[5,12], Paola Caselli[10], Emmanuel Caux[13], Steven Charnley[14], Spandan Choudhury[10], Nicolas Cuello[5], Marta De Simone[5], Francois Dulieu[15], Aurora Durán[16], Lucy Evans[8,13], Cécile Favre[5], Davide Fedele[8,17], Siyi Feng[18], Francesco Fontani[8,10], Logan Francis[19,20], Tetsuya Hama[21,22], Tomoyuki Hanawa[23], Eric Herbst[24], Shingo Hirano[9], Tomoya Hirota[25], Andrea Isella[26], Izaskun Jímenez-Serra[27], Doug Johnstone[19,20], Claudine Kahane[5], Romane Le Gal[5,28], Laurent Loinard[16,29], Ana López-Sepulcre[5,28], Luke T. Maud[30], María José Maureira[10], Francois Menard[5], Seyma Mercimek[8,31], Anna Miotello[30], George Moellenbrock[3], Shoji Mori[32], Nadia M. Murillo[7], Riouhei Nakatani[7], Hideko Nomura[33], Yasuhiro Oba[34], Ross O'Donoghue[35], Satoshi Ohashi[7], Yuki Okoda[1,7], Juan Ospina-Zamudio[5], Jaime Pineda[10], Linda Podio[8], Albert Rimola[36], Takeshi Sakai[37], Dominique Segura-Cox[10], Yancy Shirley[38], Vianney Taquet[8], Leonardo Testi[8,30], Charlotte Vastel[13], Naoki Watanabe[34], Yoshimasa Watanabe[39], Arezu Witzel[5], Ci Xue[24,40], Bo Zhao[10], and Satoshi Yamamoto[1,2]

[1] Department of Physics, The University of Tokyo, 7-3-1, Hongo, Bunkyo-ku, Tokyo 113-0033, Japan; oya@taurus.phys.s.u-tokyo.ac.jp
[2] Research Center for the Early Universe, The University of Tokyo, 7-3-1, Hongo, Bunkyo-ku, Tokyo 113-0033, Japan
[3] National Radio Astronomy Observatory, P.O. Box O, Socorro, NM 87801, USA
[4] Institute of Astronomy and Astrophysics, Academia Sinica, 11F of Astronomy-Mathematics Building, AS/NTU No. 1, Sec. 4, Roosevelt Rd., Taipei 10617, Taiwan, R.O.C.
[5] Univ. Grenoble Alpes, CNRS, IPAG, F-38000 Grenoble, France
[6] Leiden Observatory, Leiden University, P.O. Box 9513, NL02300 RA, Leiden, The Netherlands
[7] RIKEN Cluster for Pioneering Research, 2-1, Hirosawa, Wako-shi, Saitama 351-0198, Japan
[8] INAF, Osservatorio Astrofisico di Arcetri, Largo E. Fermi 5, I-50125, Firenze, Italy
[9] Department of Astronomy, The University of Tokyo, 7-3-1 Hongo, Bunkyo-ku, Tokyo 113-0033, Japan
[10] Center for Astrochemical Studies, Max-Planck-Institut für extraterrestrische Physik (MPE), Gieβenbachstr. 1, D-85741 Garching, Germany
[11] Department of Chemistry, Biology, and Biotechnology, The University of Perugia, Via Elce di Sotto 8, I-06123 Perugia, Italy
[12] Departament de Física Quántica i Astrofísica, Institut de Ciéncies del Cosmos, Universitat de Barcelona (IEEC-UB), Martí i Franqués, 1, E-08028, Barcelona, Catalunya, Spain
[13] IRAP, Université de Toulouse, CNRS, CNES, UPS, Toulouse, France
[14] Astrochemistry Laboratory, Code 691, NASA Goddard Space Flight Center, 8800 Greenbelt Rd., Greenbelt, MD 20771, USA
[15] CY Cergy Paris Université, Sorbonne Université, Observatoire de Paris, PSL University, CNRS, LERMA, F-95000, Cergy, France
[16] Instituto de Radioastronomía y Astrofísica, Universidad Nacional Autónoma de México, A.P. 3-72 (Xangari), 8701, Morelia, Mexico
[17] INAF, Osservatorio Astrofisico di Torino, Via Osservatorio 20, I-10025, Pino Torinese, Italy
[18] Department of Astronomy, Xiamen University, Xiamen, Fujian 361005, People's Republic of China
[19] NRC Herzberg Astronomy and Astrophysics, 5071 West Saanich Rd., Victoria, BC, V9E 2E7, Canada
[20] Department of Physics and Astronomy, University of Victoria, Victoria, BC, V8P 5C2, Canada
[21] Komaba Institute for Science, The University of Tokyo, 3-8-1 Komaba, Meguro, Tokyo 153-8902, Japan
[22] Department of Basic Science, The University of Tokyo, 3-8-1 Komaba, Meguro, Tokyo 153-8902, Japan
[23] Center for Frontier Science, Chiba University, 1-33 Yayoi-cho, Inage-ku, Chiba 263-8522, Japan
[24] Department of Chemistry, University of Virginia, McCormick Rd., P.O. Box 400319, Charlottesville, VA 22904, USA
[25] National Astronomical Observatory of Japan, Osawa 2-21-1, Mitaka-shi, Tokyo 181-8588, Japan
[26] Department of Physics and Astronomy, Rice University, 6100 Main St., MS-108, Houston, TX 77005, USA
[27] Centro de Astrobiología (CSIC-INTA), Ctra. de Torrejón a Ajalvir, km 4, E-28850, Torrejón de Ardoz, Spain
[28] Institut de Radioastronomie Millimétrique, F-38406 Saint-Martin d'Hères, France
[29] Instituto de Astronomía, Universidad Nacional Autónoma de México, Ciudad Universitaria, A.P. 70-264, Ciudad de México 04510, Mexico
[30] European Southern Observatory, Karl-Schwarzschild Str. 2, D-85748 Garching bei München, Germany
[31] Università degli Studi di Firenze, Dipartimento di Fisica e Astronomia, via G. Sansone 1, I-50019 Sesto Fiorentino, Italy
[32] Astronomical Institute, Graduate School of Science, Tohoku University, 6-3 Aoba, Aramaki, Aoba-ku, Sendai, Miyagi, 980-8578, Japan
[33] Division of Science, National Astronomical Observatory of Japan, 2-21-1 Osawa, Mitaka, Tokyo 181-8588, Japan
[34] Institute of Low Temperature Science, Hokkaido University, N19W8, Kita-ku, Sapporo, Hokkaido 060-0819, Japan
[35] Department of Physics and Astronomy, University College London, Gower St., London, WC1E 6BT, UK
[36] Departament de Química, Universitat Autònoma de Barcelona, E-08193 Bellaterra, Spain
[37] Graduate School of Informatics and Engineering, The University of Electro-Communications, Chofu, Tokyo 182-8585, Japan
[38] Steward Observatory, 933 N. Cherry Ave., Tucson, AZ 85721 USA
[39] Materials Science and Engineering, College of Engineering, Shibaura Institute of Technology, 3-7-5 Toyosu, Koto-ku, Tokyo 135-8548, Japan
[40] Department of Chemistry, Massachusetts Institute of Technology, 77 Massachusetts Avenue, Cambridge, MA 02139, USA
Received 2022 February 9; revised 2022 June 8; accepted 2022 June 9; published 2022 July 26

[41] Jansky Fellow of the National Radio Astronomy Observatory.

Abstract

The chemical diversity of low-mass protostellar sources has so far been recognized, and environmental effects are invoked as its origin. In this context, observations of isolated protostellar sources without the influence of nearby objects are of particular importance. Here, we report the chemical and physical structures of the low-mass Class 0 protostellar source IRAS 16544−1604 in the Bok globule CB 68, based on 1.3 mm Atacama Large Millimeter/submillimeter Array observations at a spatial resolution of ∼70 au that were conducted as part of the large program FAUST. Three interstellar saturated complex organic molecules (iCOMs), CH_3OH, $HCOOCH_3$, and CH_3OCH_3, are detected toward the protostar. The rotation temperature and the emitting region size for CH_3OH are derived to be 131 ± 11 K and ∼10 au, respectively. The detection of iCOMs in close proximity to the protostar indicates that CB 68 harbors a hot corino. The kinematic structure of the $C^{18}O$, CH_3OH, and OCS lines is explained by an infalling–rotating envelope model, and the protostellar mass and the radius of the centrifugal barrier are estimated to be 0.08–0.30 $M_\odot$ and <30 au, respectively. The small radius of the centrifugal barrier seems to be related to the small emitting region of iCOMs. In addition, we detect emission lines of c-C_3H_2 and CCH associated with the protostar, revealing a warm carbon-chain chemistry on a 1000 au scale. We therefore find that the chemical structure of CB 68 is described by a hybrid chemistry. The molecular abundances are discussed in comparison with those in other hot corino sources and reported chemical models.

Unified Astronomy Thesaurus concepts: Interstellar molecules (849); Star formation (1569); Circumstellar disks (235)

1. Introduction

The chemical evolution from protostellar cores to protoplanetary disks remains an open problem of fundamental significance to understanding the material origin of the solar system. In the last decade, significant diversity in the chemical composition of protostellar cores on a scale of a few thousand astronomical units has been revealed (Sakai & Yamamoto 2013). Two distinct cases are found: (1) a hot corino chemistry, which is characterized by a richness of (saturated) interstellar complex organic molecules (iCOMs; Cazaux et al. 2003; Herbst & van Dishoeck 2009; Caselli & Ceccarelli 2012), and (2) a warm carbon-chain chemistry (WCCC), which is characterized by a richness of (highly unsaturated) hydrocarbons such as carbon-chain molecules (Sakai et al. 2008). The chemical diversity of protostellar disks has been investigated extensively, and it is now known that the diversity in initial chemical conditions seen on core scales is inherited on disk scales (Sakai et al. 2014a; Oya et al. 2016, 2018a). Such chemical diversity on core scales could originate from various environmental effects. The source location in a molecular cloud complex and association with nearby sources in particular can significantly affect the chemical composition (Lindberg et al. 2015; Spezzano et al. 2016; Higuchi et al. 2018; Oya et al. 2019). In order to understand the basic chemical evolution of protostellar sources, the investigation of isolated sources, not affected by nearby (proto)stellar feedback, is of fundamental importance. Isolated protostellar sources are ideal laboratories not only for testing star formation theory (e.g., Evans et al. 2015) but also for testing theories of chemical evolution.

Recently, the chemical and physical characteristics of the representative isolated protostellar source B335 have been investigated with interferometric observations (Imai et al. 2016, 2019). It was reported that B335 is characterized by a very compact distribution of iCOMs and a rather extended distribution of carbon-chain molecules. These properties are consistent with a hybrid chemistry composed of both hot corino chemistry and WCCC on different scales. Similar features have also been reported for L483 (Oya et al. 2017), and are consistent with the predictions of chemical network calculations of the gas–grain model (Aikawa et al. 2008). Moreover, the envelope gas in B335 is found to be in near freefall with a very small rotation structure (∼10 au) recently identified (Bjerkeli et al. 2019; Imai et al. 2019). Now, it is important to examine whether these chemical and physical features found in B335 are also found in other isolated protostellar sources.

We are conducting the Atacama Large Millimeter/submillimeter Array (ALMA) large program FAUST (Fifty AU Study of the Chemistry in the Disk/Envelope System of Solar-like Protostars), exploring the physical and chemical structures on a 50 au scale toward 13 nearby young protostellar sources with the same brightness sensitivity (Bianchi et al. 2020; Codella et al. 2021; Okoda et al. 2021a; Ohashi et al. 2022). By observing more than 40 molecular species, FAUST systematically compares the physical and chemical structures of various types of sources. Observations of isolated sources are essential for this program.

CB 68 (L146) is a small, nearby, slightly comet-shaped opaque Bok globule located in the outskirts of the Ophiuchus molecular cloud complex (Nozawa et al. 1991; Lemme et al. 1996; Launhardt & Henning 1997; Launhardt et al. 1998). The canonical distance to the Ophiuchus molecular cloud complex of 160 pc has been used historically (Chini 1981; Launhardt & Henning 1997; Launhardt et al. 2010). However, Lombardi et al. (2008) reported the distance to the Ophiuchus molecular cloud complex to be 119 ± 6 pc by using the Hipparcos and Tycho parallax measurements with the Two Micron All Sky Survey data. Ortiz-Leon et al. (2017) reported a distance of 137.3 ± 1.2 pc based on the Very Long Baseline Array maser parallax measurements and recommended the distance of 120−140 pc. Recently, Zucker et al. (2019) derived the distance to be 144 ± 7 pc based on extinction and parallax measurements by using Gaia data. Although controversy remains, we assume that CB 68 belongs to the Ophiuchus molecular cloud complex, and use the distance of 140 pc in this paper.

CB 68 is a well-isolated protostellar source among the 32 sources in the catalog of Bok globules by Launhardt et al. (2010). Since CB 68 has a simple structure and can be accessed from ALMA, we selected this source as a target source of the FAUST program. The extent of the parent cloud core is about 0.03 pc, and its mass is estimated to be ∼0.9 $M_\odot$ (Bertrang et al. 2014). It harbors the Class 0 low-mass protostar IRAS 16544−1604, whose bolometric temperature and bolometric luminosity are 41 K and 0.86 $L_\odot$, respectively (Launhardt et al. 2013).

The protostar IRAS 16544−1604 has been monitored in the mid-IR by NEOWISE (Mainzer et al. 2014) over the last seven years. As part of a mid-IR analysis of all known Gould Belt young stellar objects, it was classified as an irregular variable by Park et al. (2021) in that the observed variability across the 14 NEOWISE epochs is greater than three times the variability seen within an individual epoch. No near-IR source is detected at 2.2 μm (Launhardt et al. 2010), indicating that no evolved protostars are associated with the globule. The protostar drives a collimated bipolar molecular outflow at position angle (P.A.) 142° (Wu et al. 1996; Vallée et al. 2000). In spite of these previous works, its detailed chemical and physical structures on scales of a few hundred astronomical units or less are little understood. In this paper, we report the first chemical and physical characterization of this source on scales of 50 to 1000 au.

The paper is organized as follows. After descriptions of observations in Section 2, we present and discuss the chemical structure in Section 3, where we compare the results with those for other low-mass protostellar sources and with those of gas–grain chemical models. Section 4 describes the kinematic structure around the protostar, and Section 5 a comparison of the chemical and physical features of CB 68 with those of the other isolated source B335. Finally, Section 6 summarizes our main findings.

2. Observations

Observations of CB 68 were conducted with ALMA (Cycle 6) in several sessions from 2018 October 4 to 2019 April 17 in the C43-1, C43-4, and Atacama Compact Array (ACA) configurations, as part of the large program FAUST (2018.1.01205.L). The field center is ($\alpha_{\rm ICRS}$, $\delta_{\rm ICRS}$) = ($16^{\rm h}57^{\rm m}19^{\rm s}.644$, $-16°09'23''.936$). Two frequency settings in Band 6, 216−234 GHz (Setup 1: 1.3 mm) and 245−260 GHz (Setup 2: 1.2 mm), were observed, where the ACA was employed to ensure a maximum recoverable size of ∼27″ (∼3800 au). The correlator was configured to observe 13 spectral windows. The spectral window used for broad continuum coverage in the observations has a bandwidth of 1875 MHz and a channel width of 0.977 MHz. This channel width corresponds to a velocity resolution of ∼1.25 km s^{-1} and ∼1.19 km s^{-1} for Setup 1 and Setup 2, respectively. The other 12 spectral windows were optimized for targeting specific molecular line transitions. These windows have a bandwidth of 58.6 MHz and a spectral resolution of 141 kHz. The channel width for the high-resolution windows corresponds to a velocity resolution of ∼0.19 km s^{-1} and ∼0.17 km s^{-1} for Setup 1 and Setup 2, respectively.

The Common Astronomy Software Applications (CASA) package (McMullin et al. 2007) was used for data reduction and imaging. The data were calibrated using a modified version of the ALMA calibration pipeline in CASA v5.6.1-8, with an additional in-house calibration routine to correct for the system temperature and spectral line data normalization.[42] Common line-free frequencies across all configurations of a setup were carefully selected and used to form a continuum data set, which was then used for self-calibration. The phase self-calibration used a solution interval as short as possible to correct for tropospheric and systematic phase errors, while avoiding noisy solutions (typically 6 to 20 s). Long solution interval amplitude and phase self-calibration was also used to align amplitudes and positions across multiple data sets. The complex gain solutions were applied to the line visibilities, and the model of the continuum emission from the self-calibration was then subtracted from the line data, to produce self-calibrated, continuum-subtracted line data. The uncertainty in the absolute flux density scale is approximately 10%.

Maps of the spectral line emission were obtained by CLEANing the dirty images with a Briggs robustness parameter of 0.5. The observation parameters of the line emission are summarized in Table 1. The line parameters were taken from the Cologne Database for Molecular Spectroscopy (Endres et al. 2016) and the Jet Propulsion Laboratory catalog (Pickett et al. 1998).

3. Chemical Structure

3.1. Dust Continuum Emission

Figure 1 shows the 1.3 mm continuum map, whose beam size is $0''.47 \times 0''.39$ (P.A.: $-65°.2$). This has a higher angular resolution than the 1.2 mm continuum map, and hence, we here use the 1.3 mm data in the present study. The continuum emission is concentrated around the protostar. The peak position determined by a 2D Gaussian fit is ($\alpha_{\rm ICRS}$, $\delta_{\rm ICRS}$) = ($16^{\rm h}57^{\rm m}19^{\rm s}.647$, $-16°09'23''.94$). The integrated flux density and peak flux density are 55.9 ± 1.1 mJy and 47.1 ± 0.6 mJy beam^{-1}, respectively. The peak intensity corresponds to a brightness temperature of 5.73 ± 0.07 K. The source image size is ($0''.473 \pm 0''.006$) × ($0''.459 \pm 0''.005$) with a P.A. of $123° \pm 16°$. This corresponds to a linear size of (66.2 ± 0.8) au × (64.2 ± 0.8) au. Since the image size is comparable to the beam size, the deconvolution is not successful. The source is very compact. Detailed analyses of the dust emission will be described in a separate publication of FAUST.

3.2. Molecular Distributions

Figure 2(a) shows the integrated intensity map of the $C^{18}O$ ($J = 2 - 1$) line. The distribution of $C^{18}O$ traces the protostellar core on a scale of 4″ (560 au) around the protostar with its intensity peak coinciding with the continuum position. Figures 2(b) and (c) show the integrated intensity maps of the unsaturated hydrocarbon molecule lines, c-C_3H_2 ($6_{0,6} - 5_{1,5}$, $6_{1,6} - 5_{0,5}$) and CCH ($N = 3 - 2$, $J = 7/2 - 5/2$), respectively. The overall extent of the c-C_3H_2 emission is comparable to that of $C^{18}O$, indicating that c-C_3H_2 exists in the protostellar core traced by $C^{18}O$. However, the distributions are different between c-C_3H_2 and $C^{18}O$. The c-C_3H_2 emission does not peak at the continuum peak position but shows a rather extended structure to the northwestern and eastern directions. Moreover, the weak emission seems to extend more to the northern part than to the southern part. These features can be seen more clearly in the CCH emission map. The molecular outflow is aligned along the northwest–southeast direction, and hence, the CCH emission seems to be enhanced in the outflow cavity wall, as seen in IRAS 15398–3359, L483, and NGC 1333 IRAS 4C (Oya et al. 2014, 2018b; Zhang et al. 2018). Therefore, the northwestern feature of c-C_3H_2 may also be affected by the outflow.

Figure 3(a) shows the intensity profiles of the $C^{18}O$, c-C_3H_2, CCH, and continuum emission along a line passing through the continuum peak with a P.A. of 232°. This direction is perpendicular to the P.A. of the previously reported outflow (Wu et al. 1996; Vallée et al. 2000), and hence, Figure 3(a)

[42] See https://help.almascience.org/index.php?/Knowledgebase/Article/View/419.

Table 1
Parameters for Used Lines

Molecule	Transition	Frequency (MHz)	$S\mu^2$ (D^2)	E_u (K)	W[a] (Jy beam^{-1} km s^{-1})	Maj[b] (arcsec)	Min[b] (arcsec)
$C^{18}O$	$J = 2 - 1$	219,560.3541	0.0244	15.8060	0.218(7)	0.491	0.411
c-C_3H_2	$6_{0,6} - 5_{1,5}$	217,822.1480	58.3	38.6077	0.037(6)[c]	0.502	0.411
	$6_{1,6} - 5_{0,5}$	217,822.1480	175	...	...	...	...
CCH	$N = 3 - 2$, $J = 7/2 - 5/2$, $F = 4 - 3$	262,004.2600	2.29	25.1494	0.071(7)[c]	0.551	0.476
	$N = 3 - 2$, $J = 7/2 - 5/2$, $F = 3 - 2$	262,006.4820	1.71	25.1482	...	...	...
CH_3OH	$4_{2,3} - 3_{1,2}$ E	218,440.0630	3.47	45.4600	0.162(6)	0.497	0.409
	$5_{1,4} - 4_{1,3}$ A	243,915.7880	3.88	49.6607	0.209(6)	0.591	0.506
	$10_{3,7} - 11_{2,9}$ E	232,945.7970	3.04	190.3713	0.091(6)	0.470	0.388
	$18_{3,15} - 17_{4,14}$ A	233,795.6660	5.47	446.5851	0.051(7)	0.469	0.388
	$4_{2,3} - 5_{1,4}$ A	234,683.3700	1.12	60.9237	0.117(6)	0.467	0.387
	$5_{4,2} - 6_{3,3}$ E	234,698.5190	0.46	122.7230	0.047(6)	0.467	0.387
	$20_{3,17} - 20_{2,18}$ A	246,074.6050	19.5	537.0395	0.098(5)	0.587	0.503
	$19_{3,16} - 19_{2,17}$ A	246,873.3010	18.4	490.6542	0.102(6)	0.586	0.502
	$16_{2,15} - 15_{3,13}$ E	247,161.9500	4.83	338.1423	0.091(7)	0.585	0.501
	$4_{2,2} - 5_{1,5}$ A	247,228.5870	1.09	60.9253	0.144(6)	0.584	0.500
	$18_{3,15} - 18_{2,16}$ A	247,610.9180	17.4	446.5852	0.116(7)	0.584	0.500
$HCOOCH_3$	$19_{4,16} - 18_{4,15}$ A	233,226.7880	48.0	123.2487	0.030(6)	0.470	0.388
	$18_{4,14} - 17_{4,13}$ E	233,753.9600	45.8	114.3711	0.028(7)	0.468	0.387
	$18_{4,14} - 17_{4,13}$ A	233,777.5210	45.8	114.3651	0.021(7)	0.469	0.388
	$20_{13,7} - 19_{13,6}$ E	245,883.1790	92.5	235.9818	0.047(6)[c]	0.588	0.504
	$20_{13,7} - 19_{13,6}$ A	245,885.2430	...	...	...	...	...
	$20_{13,8} - 19_{13,7}$ A	245,885.2430	...	...	...	...	...
	$20_{11,9} - 19_{11,8}$ E	246,285.4000	37.2	204.2141	0.031(6)	0.587	0.503
	$20_{11,10} - 19_{11,9}$ A	246,295.1350	74.4	204.2103	0.039(6)[c]	0.586	0.502
	$20_{11,9} - 19_{11,8}$ A	246,295.1350	...	...	...	...	...
	$20_{11,10} - 19_{11,9}$ E	246,308.2720	37.2	204.2014	0.027(6)	0.586	0.502
	$20_{10,10} - 19_{10,9}$ E	246,600.0120	40.0	190.3465	0.039(6)	0.586	0.502
	$20_{10,11} - 19_{10,10}$ A	246,613.3920	80.0	190.3410	0.054(6)[c]	0.586	0.502
	$20_{10,10} - 19_{10,9}$ A	246,613.3920	...	...	...	...	...
	$20_{10,11} - 19_{10,10}$ E	246,623.1900	40.0	190.3340	0.032(6)	0.586	0.502
CH_3OCH_3	$14_{1,14} - 13_{0,13}$ EA	258,548.8190	679	93.3326	0.082(7)[c]	0.561	0.480
	$14_{1,14} - 13_{0,13}$ AE	258,548.8190	...	...	...	...	...
	$14_{1,14} - 13_{0,13}$ EE	258,549.0630	...	...	...	...	...
	$14_{1,14} - 13_{0,13}$ AA	258,549.3080	...	...	...	...	...
	$18_{5,13} - 18_{4,14}$ AE	257,911.0360	357	190.9744	0.058(8)[c]	0.560	0.481
	$18_{5,13} - 18_{4,14}$ EA	257,911.1750	...	...	...	...	...
	$18_{5,13} - 18_{4,14}$ EE	257,913.3120	...	...	...	...	...
OCS	$J = 19 - 18$	231,060.9934	9.72	110.8999	0.159(6)	0.470	0.391
CH_2DOH	$8_{2,6} - 8_{1,7}$ e_0	234,471.0333	9.55	93.6659	0.043(6)	0.467	0.387
	$4_{1,4} - 4_{1,3}$ e_1–e_0	246,973.1071	1.10	37.6942	0.031(5)	0.585	0.501
	$3_{2,1} - 3_{1,2}$ e_0	247,625.7463	2.36	29.0149	0.027(7)	0.584	0.500
	$5_{2,4} - 5_{1,5}$ e_0	261,687.3662	4.01	48.3132	0.043(7)	0.553	0.477
NH_2CHO	$12_{0,12} - 11_{0,11}$	247,390.7190	156	78.1227	<0.007	0.585	0.501
CH_3CHO	$11_{1,10} - 10_{1,9}$ E	216,581.9304	69.0	64.8710	<0.006	0.504	0.417
C_2H_5OH	$14_{3,11} - 13_{3,10}$	246,414.7897	21.6	155.7234	<0.006	0.587	0.503
C_2H_5CN	$27_{2,25} - 26_{2,24}$	246,268.7367	398	169.8051	<0.006	0.587	0.503
CH_3COCH_3	$23_{2,21} - 22_{2,20}$	247,562.2435	2428	153.3326	<0.007[c]	0.585	0.500
	$23_{2,21} - 22_{3,20}$	247,562.2435	323	...	...	...	...
	$23_{3,21} - 22_{2,20}$	247,562.2435	323	...	...	...	...
	$23_{3,21} - 22_{3,20}$	247,562.2435	2428	...	...	...	...
HCOOH	$11_{2,10} - 10_{2,9}$	246,105.9739	21.5	83.7410	<0.006	0.587	0.503
$CH_2(OH)CHO$	$23_{0,23} - 22_{1,22}$	233,037.3570	117	136.5843	<0.006[c]	0.470	0.388
	$23_{1,23} - 22_{0,22}$	233,037.7300	117	136.5847	...	...	...

Notes.
[a] Integrated intensity. Numbers in parentheses represent 1σ, which applies to the last significant digits. The upper limit also represents 1σ.
[b] Synthesized beam size. The P.A. is 112°–114° for Setup 1 (216–234 GHz) and 93°–95° for Setup 2 (245–260 GHz).
[c] Total integrated intensity over blended lines.

reveals the intensity profile along the disk/envelope system. The intensities of c-C_3H_2 and CCH tend to increase approaching the protostar, although that of CCH seems heavily affected by the outflow. The association of c-C_3H_2 and CCH with the protostar on a 1000 au scale indicates that CB 68 is characterized by a WCCC (e.g., Aikawa et al. 2008; Sakai et al. 2008; Sakai & Yamamoto 2013). For reference, the intensity profiles along the outflow direction are shown in

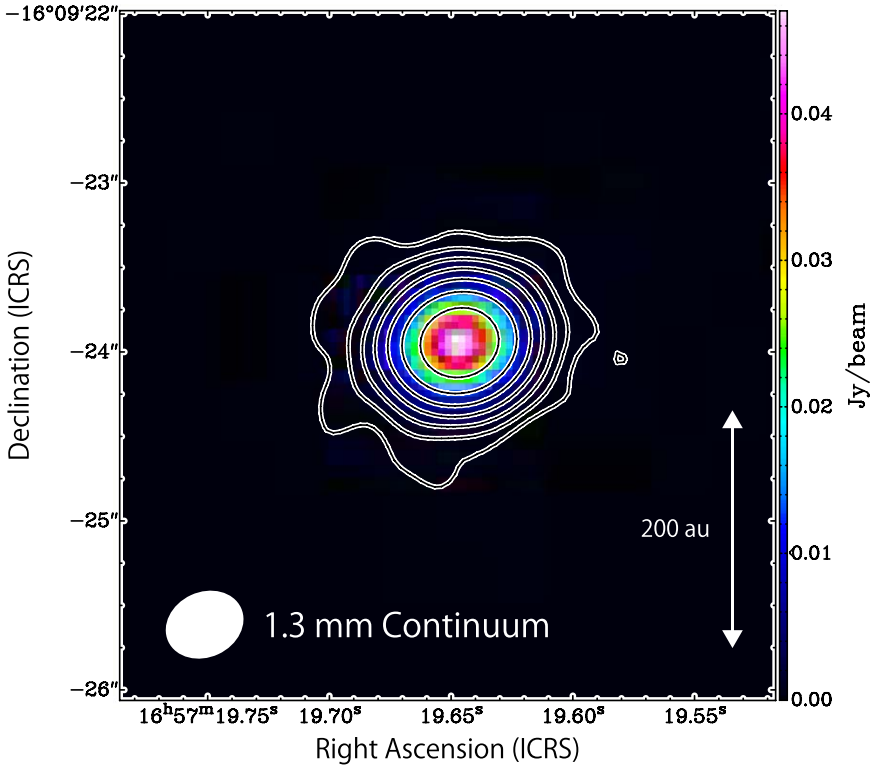

Figure 1. Image of the 1.3 mm dust continuum. The peak position is $(\alpha_{\rm ICRS}, \delta_{\rm ICRS}) = (16^{\rm h}57^{\rm m}19\overset{\rm s}{.}647, -16°9'23\overset{''}{.}94)$. The rms noise level ($\sigma$) is 40 μJy beam^{-1}. The contour levels start at 10σ and double in value up to 640σ. A white ellipse represents the beam size.

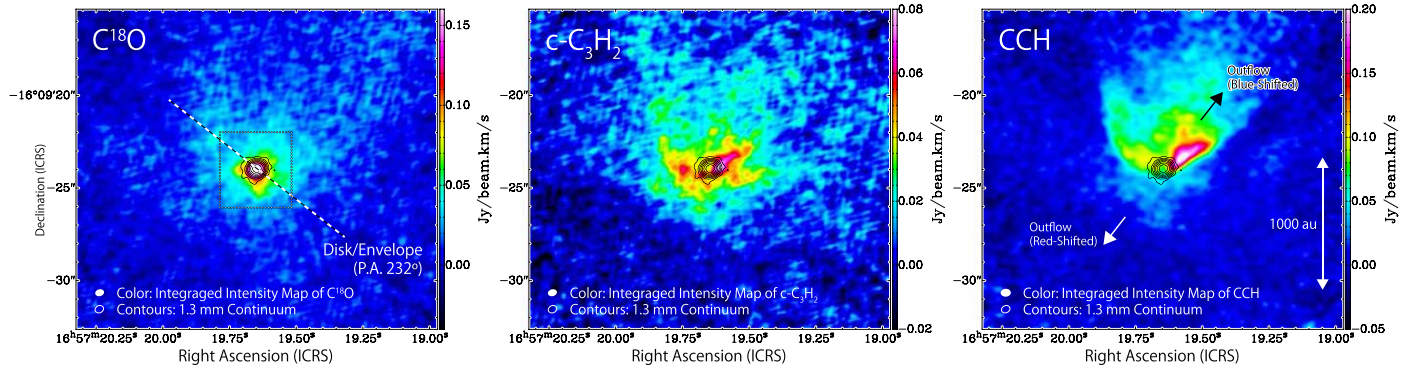

Figure 2. Integrated intensity maps (moment 0 maps) of $C^{18}O$ ($J = 2 - 1$), c-C_3H_2 ($6_{0,6} - 5_{1,5}$; $6_{1,6} - 5_{0,5}$), and CCH ($N = 3 - 2$, $J = 7/2 - 5/2$) (color) and the continuum image (black contours; Figure 1). The integrated velocity range is 0.0 km s^{-1} to 9.8 km s^{-1} for the three lines, where the systemic velocity is 5.0 km s^{-1}. A dashed line on the left panel indicates the direction of the disk/envelope system, which is perpendicular to the CO outflow direction (P.A. 142°) (Wu et al. 1996; Vallée et al. 2000). The rms noise level is 7 mJy beam^{-1} km s^{-1} for the three maps. A dashed rectangle in the $C^{18}O$ panel indicates the area for Figures 1, 5, 9, and 10. The beam sizes are shown in the bottom left corner of each panel.

Figure 3(b). Although the distribution of c-C_3H_2 is centrally concentrated, the CCH emission shows an extension to the northwestern side along the outflow. Such extension is seen in the integrated intensity map of Figure 2(c).

The fractional abundance of c-C_3H_2 relative to H_2 at the continuum peak position is derived in the following way. Here, we use the $C^{18}O$ emission to derive the H_2 column density. Figure 4(a) shows the spectra of c-C_3H_2 and $C^{18}O$ at the continuum position. The spectrum of c-C_3H_2 shows self-absorption of the redshifted component due to an infalling motion and of the systemic velocity component due to the foreground gas (e.g., Evans et al. 2015; Yang et al. 2020). To minimize these effects, we conservatively employ the blue-shifted component, which is less affected by these factors, in the fractional abundance derivation. The peak intensities of the blueshifted emission measured by the Gaussian fit are 32 mJy beam^{-1} and 54 mJy beam^{-1} for c-C_3H_2 and $C^{18}O$, respectively. From these values, the column densities of the blueshifted component of c-C_3H_2 and $C^{18}O$ are derived to be $(2.4 - 3.5) \times 10^{13}$ cm^{-2} and 5.4×10^{15} cm^{-2}, respectively, by using the non-LTE radiative transfer code RADEX. For this calculation the line width of 1.05 km s^{-1} is used for both species, and H_2 volume densities of 10^6–10^8 cm^{-3} are assumed. This is the range of H_2 densities for a typical protostellar envelope (Sakai et al. 2014b). The gas kinetic temperature is uncertain. We adopt 25 K for it, which is the desorption temperature of CH_4 for triggering WCCC (Sakai et al. 2008; Sakai & Yamamoto 2013). The column density for each species is derived to match the intensity calculated by RADEX with the observed one. The maximum optical depths

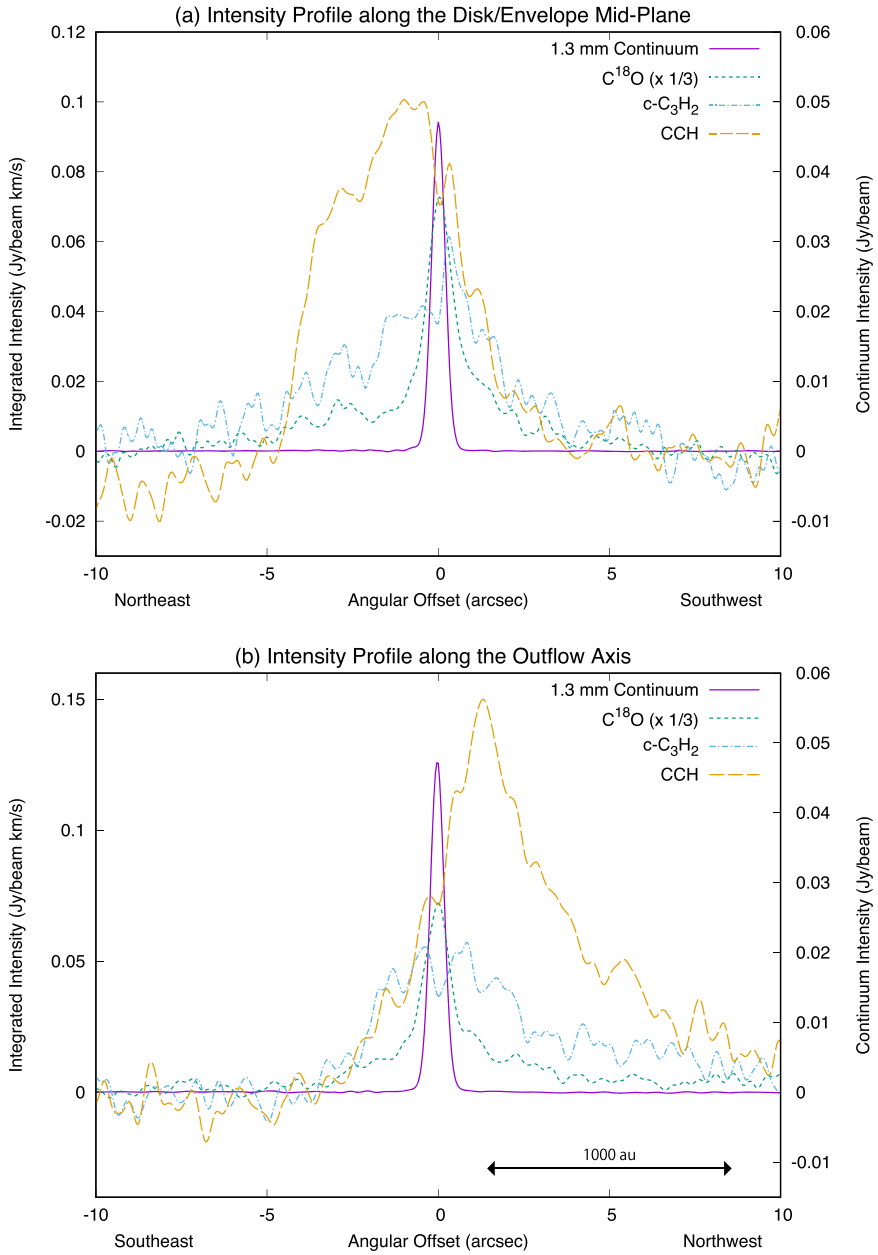

Figure 3. (a) Intensity profiles of the $C^{18}O$ ($J = 2 - 1$), c-C_3H_2 ($6_{0,6} - 5_{1,5}$; $6_{1,6} - 5_{0,5}$), CCH ($N = 3 - 2$, $J = 7/2 - 5/2$), and 1.3 mm dust continuum emission along the disk/envelope direction (P.A. 232°) indicated in the left panel of Figure 2 and (b) those along the outflow axis (P.A. 142°). The position is the offset from the continuum peak position. The rms noise level is 7 mJy beam^{-1} km s^{-1} for the $C^{18}O$, c-C_3H_2, and CCH lines, while it is 40 μJy beam^{-1} for the continuum emission.

of the c-C_3H_2 and $C^{18}O$ lines are 0.55 and 0.42, respectively. Then, the fractional abundance of c-C_3H_2 relative to H_2 is roughly estimated to be (0.7–1.0) $\times 10^{-9}$, where the H_2 column density is evaluated from the $C^{18}O$ column density to be $\sim 3.6 \times 10^{22}$ cm^{-2} by using the empirical equation for the high $C^{18}O$ column density case ($>3 \times 10^{14}$ cm^{-2}) reported by Frerking et al. (1982). If we assume gas kinetic temperatures of 15 K and 35 K, the fractional abundances of c-C_3H_2 are (0.8–2.1) $\times 10^{-9}$ and 0.6×10^{-9}, respectively. In this case, the maximum optical depths of c-C_3H_2 and $C^{18}O$ are 1.5 and 1.1, respectively, for the H_2 density of 10^6 cm^{-3} and the temperature of 15 K. Hence, the estimated range of the fractional abundance of c-C_3H_2 is (0.6–2.1) $\times 10^{-9}$ in CB 68, which is lower by one or two orders of magnitude than the value found for L1527 (2.7×10^{-8}) (Sakai et al. 2010).

The low abundance may originate from the above analysis focused on the protostellar position with a narrow beam ($\sim$70 au). Then, we also calculate the fractional abundance range of c-C_3H_2 averaged over a circular area 4.″0 (560 au) in diameter centered at the protostar position, which is comparable to the distribution of c-C_3H_2. Figure 4(b) shows the spectra of c-C_3H_2 and $C^{18}O$ averaged over the area. The self-absorption feature of the redshifted component and the systemic velocity component is also seen as in the above case, and hence, we employ the blueshifted component for the fractional abundance evaluation. Through the procedure mentioned above, we obtain a range of the fractional abundance of c-C_3H_2 of (0.9–4.2) $\times 10^{-9}$, which is not much different from that derived with the narrow beam. In this case, the maximum optical depths of c-C_3H_2 and $C^{18}O$ are

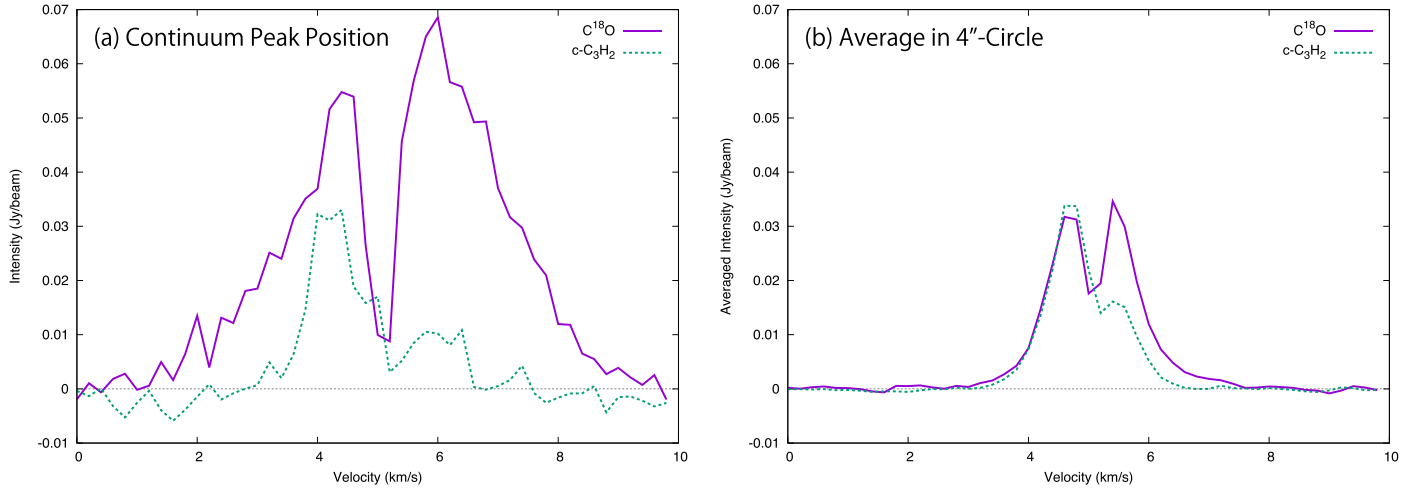

Figure 4. (a) Observed spectra of $C^{18}O$ ($J = 2 - 1$) and c-C_3H_2 ($6_{0,6} - 5_{1,5}$; $6_{1,6} - 5_{0,5}$) at the continuum position. (b) Observed spectra of $C^{18}O$ and c-C_3H_2 averaged over a circular area 4.″0 in diameter around the continuum peak.

1.6 and 0.5, respectively, for the H_2 density of 10^6 cm^{-3} and the temperature of 15 K. These analyses imply that the enhancement of the c-C_3H_2 abundance due to the WCCC effect is weaker in CB 68 than in L1527.

On the other hand, CH_3OH is concentrated around the protostar on a scale of 100 au or less, as shown in Figures 5(a) and (b), where the low-excitation line ($4_{2,3} - 3_{1,2}$ E; $E_u/k_B = 45.46$ K) and the high-excitation line ($16_{2,15} - 15_{3,13}$ E; $E_u/k_B = 338.14$ K) are depicted, respectively. Here, k_B stands for the Boltzmann constant. The CH_3OH lines show a compact distribution and are not resolved by the synthesized beam. In total, 11 lines of CH_3OH are detected (Table 1). In addition, CH_2DOH, $HCOOCH_3$, and CH_3OCH_3 are detected, as listed in Table 1. Here, the detection criterion is that the integrated intensity is higher than the 3σ noise level. To identify these molecules, we visually inspect all lines of a certain species in the observed spectral windows, confirming that the line intensities are self-consistent. For $HCOOCH_3$, there are several faint lines in the continuum bands (Figure 6), which are reasonably explained by the calculated spectrum using the column density and the rotation temperature derived below. Similarly, all the intensities of the identified lines are consistent, from an a posteriori check, with the derived column densities and rotation temperatures. Examples of the moment 0 maps of $HCOOCH_3$ and CH_3OCH_3 are shown in Figures 5(c) and (d), respectively. Their distributions are compact around the protostar and are not resolved by the synthesized beam ($\sim$0.″4−0.″5; $\sim$70−80 au), as in the case of the high-excitation line of CH_3OH.

We carefully check the other iCOM lines by using their simulated spectra, as applied to the $HCOOCH_3$ lines in the above paragraph. We notice that a line at 234,471 MHz could match the $3_{3,1} - 3_{2,2}$ E line of CH_3CHO (234,469 MHz). However, this line is overlapped with the CH_2DOH line ($8_{2,6} - 8_{1,7}$ e_0; 234,471 MHz), and moreover, the other CH_3CHO lines near this line, which are expected to be of equivalent intensity or brighter, are not detected. We thus conclude that CH_3CHO is not detected in these observations. Following a similar procedure, we also conclude that NH_2CHO, C_2H_5OH, HCOOH, CH_3COCH_3, and C_2H_5CN are not detected (Table 1).

In CB 68, the carbon-chain-related species (unsaturated hydrocarbon), c-C_3H_2, is concentrated around the protostar on a scale of 1000 au, a signature of WCCC. In contrast, compact distributions of iCOMs are also found on a scale of 100 au or less, which is evidence for hot corino chemistry. Hence, CB 68 can be regarded to have a hybrid chemistry, where WCCC and hot corino chemistry coexist but on different scales. Such chemical characteristics have been found in other low-mass protostellar sources such as L483 and B335 (Imai et al. 2016; Oya et al. 2017). It is important to emphasize that the above chemical structure found in CB 68 is similar to that found in B335, which is also an isolated protostellar source. For quantitative comparison with the other sources in Section 3.4, we derive the molecular column densities in the following subsection.

3.3. Abundances of iCOMs

First, the column density (N) and the rotation temperature (T_{rot}) of CH_3OH at the continuum peak are derived under the assumption of local thermal equilibrium (LTE). The emitting region for the high-excitation lines of CH_3OH is very compact around the protostar, where the density is high enough for the LTE approximation to hold. We use the following equation that considers the effect of optical depth on the observed intensity (Yamamoto 2017):

$$T_{obs} = f\left(\frac{c^2}{2k_B\nu^2}\right)(B_\nu(T_{rot}) - B_\nu(T_b))(1 - \exp(-\tau)), \quad (1)$$

and

$$\tau = \frac{8\pi^3 S\mu^2}{3h\Delta v U(T)}\left[\exp\left(\frac{h\nu}{k_B T}\right) - 1\right]\exp\left(\frac{-E_u}{k_B T}\right)N, \quad (2)$$

where $B_\nu(T)$ denotes the Planck function, $U(T)$ the partition function of the molecules at the excitation temperature T, N the column density, ν the frequency of the line, E_u the upper-state energy, f the beam filling factor, and T_b the cosmic microwave background temperature (2.7 K).

The CH_3OH lines used in the least-squares analysis are listed in Table 1. Among them, we find that the optical depths for the two low-excitation lines ($4_{2,3} - 3_{1,2}$ E, 218,440 MHz, $E_u/k_B =$ 45.46 K; $5_{1,4} - 4_{1,3}$ A, 243,916 MHz, $E_u/k_B = 49.66$ K) are higher than 6. Conservatively, to minimize opacity effects, we use the lines for which the opacity is less than 2. The rotation

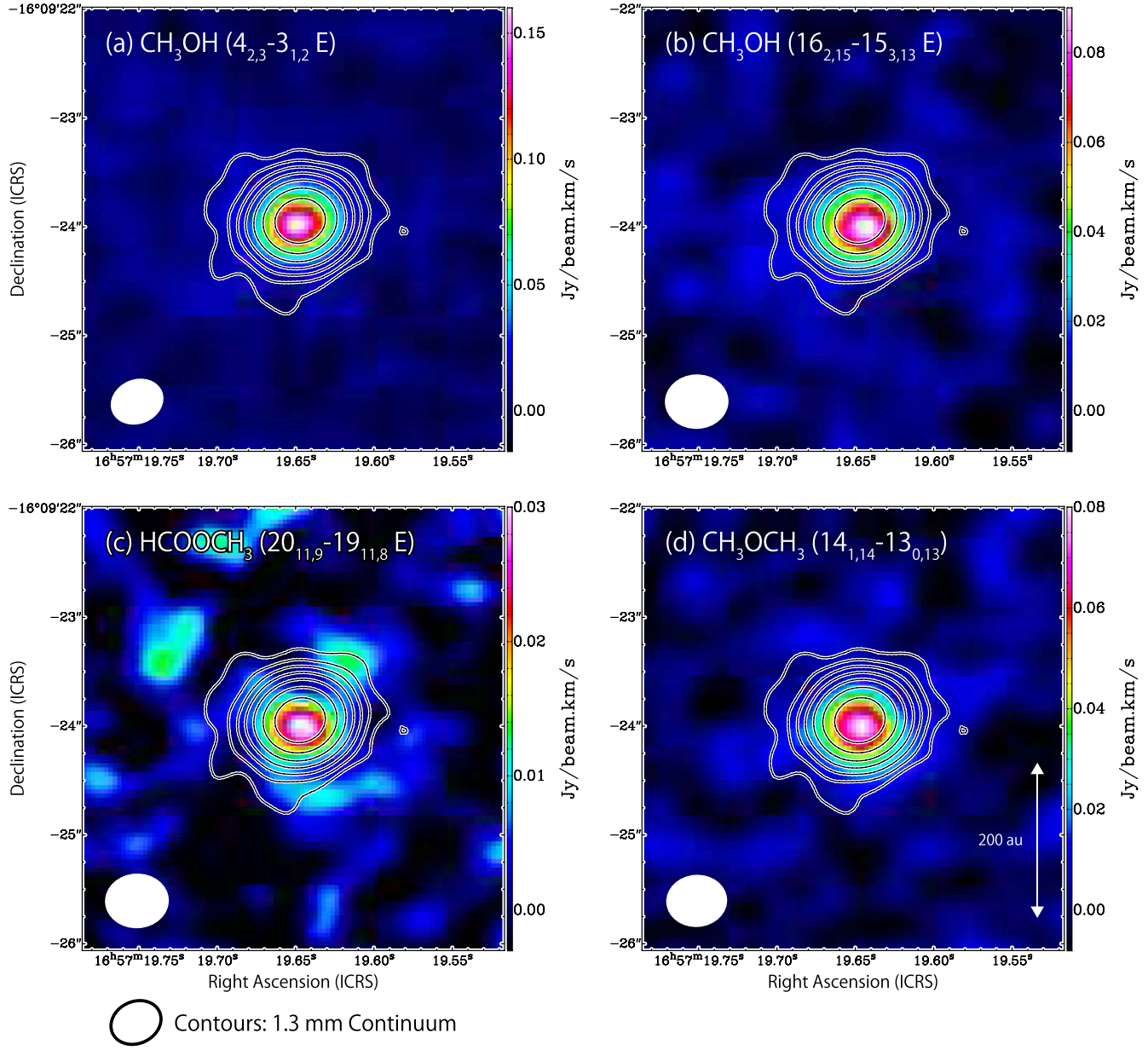

Figure 5. Integrated intensity maps (moment 0 maps) of CH_3OH ($4_{2,3} - 3_{1,2}$ E), CH_3OH (high-excitation line; $16_{2,15} - 15_{3,13}$ E), $HCOOCH_3$ ($20_{11,9} - 19_{11,8}$ E), and CH_3OCH_3 ($14_{1,14} - 13_{0,13}$ EA, AE, EE, and AA). Contours represent the continuum image of Figure 1. The rms noise level is 4 mJy beam^{-1} km s^{-1} for the CH_3OH ($4_{2,3} - 3_{1,2}$ E) line and the $HCOOCH_3$ line and 5 mJy beam^{-1} km s^{-1} for the other two lines. The velocity range for the integration is 0 to 9.8 km s^{-1} for the CH_3OH ($4_{2,3} - 3_{1,2}$ E) line and the CH_3OCH_3 line and 0 to 10.5 km s^{-1} for the other two lines. The beam sizes are shown in the bottom left corner of each panel.

temperature, the column density, and the beam filling factor are determined by the least-squares analysis on the peak intensities, which are derived by dividing the integrated intensity by the line width (6 km s^{-1}). The largest correlation coefficient between the parameters in the least-squares fit is 0.68 between the column density and the beam filling factor. Hence, the parameters are well determined in the fit. The rotation temperature and the column density are derived to be 131 ± 11 K and $(2.7 \pm 1.0) \times 10^{18}$ cm^{-2}, respectively, where the errors represent the standard deviation of the fit. The beam filling factor is well constrained and determined to be 0.022 ± 0.003. Since the high-excitation lines used in the analysis are not spatially resolved with the current synthesized beam, the small beam filling factor is reasonable. This means that the CH_3OH emission, particularly for the high-excitation lines, mainly comes from a very compact region whose size is approximately 10 au. The maximum optical depth among the fitted lines is 1.9 for the $4_{2,2} - 5_{1,5}$ A line. In Figure 6, the calculated spectrum of CH_3OH is overlaid on the two spectral windows. The observations are well reproduced by the spectrum calculated by using the best-fit parameters.

Similarly, the column density of $HCOOCH_3$ is derived using the least-squares fit on the observed lines listed in Table 1, where Equation (1) is employed. Here, heavily blended lines are excluded in the analysis. Although we try to determine the column density, the rotation temperature, and the beam filling factor simultaneously, the rotation temperature and the beam filling factor are not well determined in the fit. This is due to a relatively poor signal-to-noise ratio of the spectra. Hence, we determine the column density of $HCOOCH_3$ by assuming the rotation temperature and the beam filling factor measured for CH_3OH. This assumption is justified, because the emitting

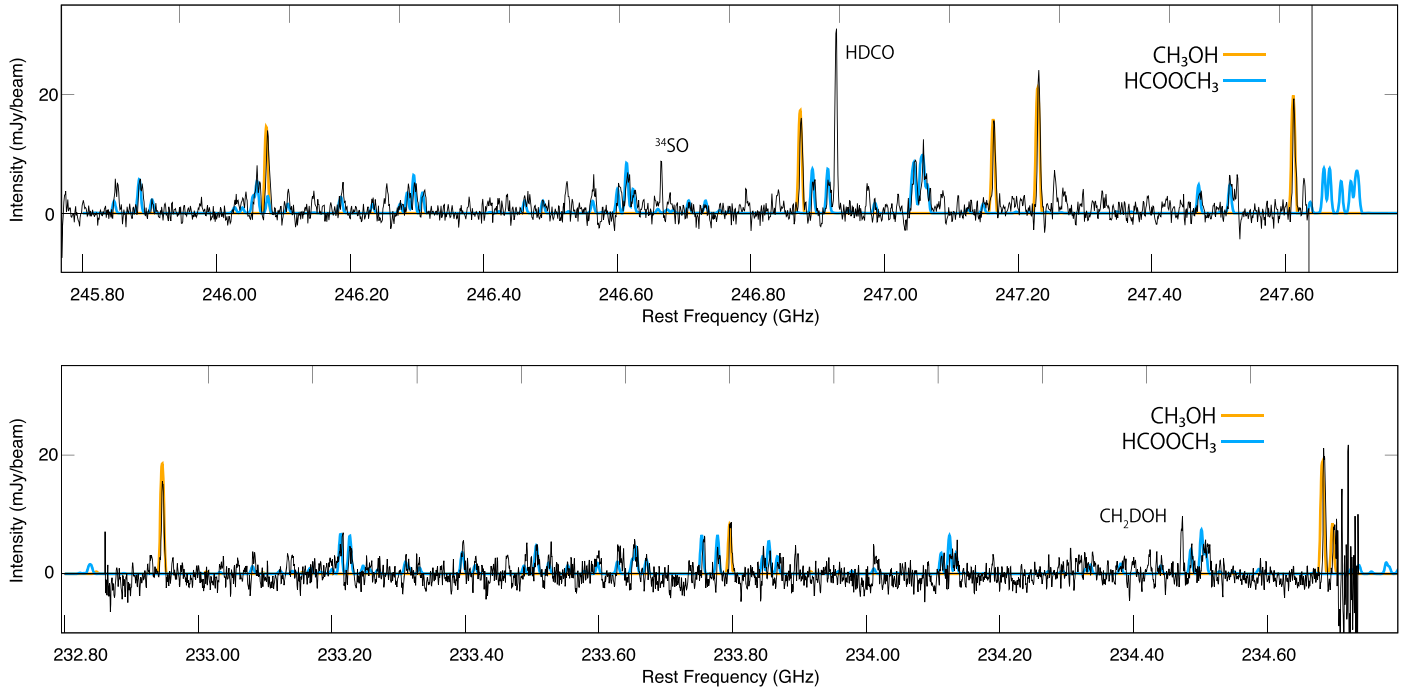

Figure 6. Observed spectra of the two continuum bands for demonstration of rich iCOM lines (black lines). A systemic velocity of 5.0 km s^{-1} is adopted to calculate the rest frequency. Colored spectra are the results of the simulation based on the column density, the rotation temperature, and the beam filling factor derived in the analysis. See Section 3.3 for details. Orange lines represent CH_3OH, whereas blue ones represent $HCOOCH_3$.

Table 2
Column Densities of iCOMs

Molecule	Column Density (cm^{-2})		
	$T = 100$ K	$T = 131$ K	$T = 150$ K
$HCOOCH_3$	$(2.2 \pm 0.4) \times 10^{17}$	$(2.3 \pm 0.3) \times 10^{17}$	$(2.4 \pm 0.3) \times 10^{17}$
CH_3OCH_3	1.5×10^{17}	1.7×10^{17}	1.9×10^{17}
CH_2DOH	1.2×10^{17}	1.5×10^{17}	1.7×10^{17}
NH_2CHO[a]	$<1.1 \times 10^{15}$	$<1.3 \times 10^{15}$	$<1.5 \times 10^{15}$
C_2H_5OH[a]	$<5.4 \times 10^{16}$	$<6.0 \times 10^{16}$	$<6.4 \times 10^{16}$
C_2H_5CN[a]	$<3.8 \times 10^{15}$	$<4.2 \times 10^{15}$	$<4.7 \times 10^{15}$
$(CH_3)_2CO$[a]	$<9.8 \times 10^{15}$	$<1.1 \times 10^{16}$	$<1.3 \times 10^{16}$
HCOOH[a]	$<6.4 \times 10^{15}$	$<7.8 \times 10^{15}$	$<8.7 \times 10^{15}$
CH_3CHO[a]	$<1.1 \times 10^{16}$	$<1.6 \times 10^{16}$	$<1.9 \times 10^{16}$
$CH_2(OH)CHO$[a]	$<7.9 \times 10^{15}$	$<8.5 \times 10^{15}$	$<8.9 \times 10^{15}$
CH_3OH[b]	...	$(2.7 \pm 1.0) \times 10^{18}$	...

Notes.
[a] Upper limits to the column densities are derived for nondetected molecules.
[b] The rotation temperature (T) is derived to be 131 ± 11 K. The beam filling factor (f) is derived to be 0.022 ± 0.003.

region of the high-excitation lines of CH_3OH and that of the $HCOOCH_3$ lines are likely to be similar (i.e., to be a hot corino). Nevertheless, we also evaluate the column density by assuming rotation temperatures of 100 K and 150 K, in order to investigate the dependence of the column density on the assumed temperature. The results are shown in Table 2. The $HCOOCH_3$ spectrum calculated for the 131 K case is overlaid on Figure 6, which is consistent with the observation.

The column densities of CH_3OCH_3 and CH_2DOH are derived in the same way for $HCOOCH_3$ discussed above (Table 2). Specifically, the rotation temperature and the beam filling factor are fixed to the values derived from CH_3OH because of small numbers of detected lines. The column densities are also evaluated assuming rotation temperatures of 100 K and 150 K. Note that the CH_2DOH ($4_{1,4} - 4_{1,3}$ e_1−e_0) line at 246,973 MHz is not included in the fit, because the line strength of this intervibrational transition is uncertain (Pickett et al. 1998). Recently, the uncertainty of the line strength for this molecule has also been pointed out by Ambrose et al. (2021).

We derive the 3σ upper limits to the column densities of NH_2CHO, CH_3CHO, C_2H_5OH, HCOOH, CH_3COCH_3, and C_2H_5CN, assuming the rotation temperature and the beam filling factor derived in the CH_3OH analysis. They are also evaluated assuming a rotation temperature of 100 and 150 K. For this purpose, we simulate the spectrum of each molecule in all the spectral windows of our observations and select the highest-intensity line for derivation of the upper limit. The upper limit to the column density is then evaluated from the 3σ upper limit to the integrated intensity. The line width is assumed to be 6 km s^{-1}. This is the average line width of the

detected iCOMs in this observation. The derived upper limits are summarized in Table 2.

3.4. Comparison with Other Sources

In this section, we compare the molecular abundances of iCOMs in CB 68 to those in several hot corinos observed with interferometers. To this end, column density ratios between iCOMs are used instead of the fractional abundance relative to H_2, because the H_2 column density for the emitting region of iCOMs is not available in this source. The $HCOOCH_3/CH_3OH$ ratio in CB 68 is derived to be $0.09^{+0.07}_{-0.03}$. This ratio is slightly higher than values found in other sources harboring a hot corino: IRAS 16293−2422 Source A ($0.021^{+0.011}_{-0.008}$; Manigand et al. 2020), IRAS 16293−2422 Source B ($0.026^{+0.008}_{-0.007}$; Jørgensen et al. 2018), NGC 1333 IRAS 2A ($0.016^{+0.012}_{-0.007}$; Taquet et al. 2015), B1-c ($0.010^{+0.005}_{-0.002}$; van Gelder et al. 2020), Ser-emb 8 ($0.011^{+0.009}_{-0.004}$; van Gelder et al. 2020), and L1551 IRS 5 (0.033 ± 0.002; Bianchi et al. 2020). The CH_2DOH/CH_3OH ratio is derived to be $0.06^{+0.04}_{-0.02}$. This is close to the corresponding ratios in other hot corinos: IRAS 16293−2422 Source A ($0.09^{+0.04}_{-0.03}$; Manigand et al. 2020), IRAS 16293−2422 Source B (0.07 ± 0.02; Jørgensen et al. 2018), B1-c ($0.08^{+0.04}_{-0.02}$; van Gelder et al. 2020), and Ser-emb 8 ($0.043^{+0.033}_{-0.014}$; van Gelder et al. 2020). It should be noted that the intrinsic line strength of CH_2DOH could be uncertain (Ambrose et al. 2021), so that the derived ratio may be changed by a factor of a few.

Since the CH_3OH abundance when considering the effect of optical depth is not always available for several hot corinos and would have a large uncertainty, the ratio relative to $HCOOCH_3$, which is likely optically thin in all the sources, is used for comparison to other iCOMs, as summarized in Table 3 and Figure 7. The $CH_3OCH_3/HCOOCH_3$ and $C_2H_5OH/HCOOCH_3$ ratios do not vary among the sources very much. Indeed, the $CH_3OCH_3/HCOOCH_3$ ratio in CB 68 is 0.74 ± 0.11, which is almost comparable to those for the other sources. A trend of a constant $CH_3OCH_3/HCOOCH_3$ ratio is also reported by Chahine et al. (2022). On the other hand, the other ratios show some variation from source to source. Although only 3σ upper limits to the ratio relative to $HCOOCH_3$ are obtained for the other species, the $CH_3CHO/HCOOCH_3$, $NH_2CHO/HCOOCH_3$, and $HCOOH/HCOOCH_3$ ratios in CB 68 tend to be low among the other hot corinos. Hence, CH_3CHO, NH_2CHO, and HCOOH seem relatively less abundant in CB 68. Such a trend for CH_3CHO and NH_2CHO can also be seen in Figure 8. In particular, the difference is significant between the two isolated sources, CB 68 and B335. Meanwhile, the upper limits to the $C_2H_5OH/HCOOCH_3$, $C_2H_5CN/HCOOCH_3$, and $CH_3COCH_3/HCOOCH_3$ ratios are comparable to the corresponding ratios in the other sources. Table 3 lists the bolometric luminosity and the bolometric temperature of each source. The deficiency of CH_3CHO, NH_2CHO, and HCOOH in CB 68 is not simply ascribed to these physical parameters.

It should be noted that the dust continuum emission can be optically thick at millimeter wavelengths. Although the beam-averaged brightness temperature of the dust emission in CB 68 is 5.73 ± 0.07 K, the dust opacity could be higher for the emitting region of CH_3OH. A detailed analysis of the dust emission is left for future study, which includes analysis of the other ALMA frequency bands. Here, we just discuss the effect of optically thick dust on the observed molecular abundances. If the emitting region is the same for all the iCOMs observed in this study, the optically thick dust would not seriously affect the above discussions on the abundance ratios. The effect is compensated for at least partially by taking the column density ratios. However, the distribution of the emission could be different from iCOM to iCOM. For instance, N-bearing iCOMs such as NH_2CHO and C_2H_5CN would be more centrally concentrated around the protostar than O-bearing iCOMs such as $HCOOCH_3$ and CH_3OCH_3, as revealed in high-mass protostellar sources (e.g., Jiménez-Serra et al. 2012; Feng et al. 2015; Csengeri et al. 2019). Such a trend has recently been found in the low-mass protostellar source L483 (Oya et al. 2017; Okoda et al. 2021b). If this were also the case for CB 68, N-bearing iCOMs would be more affected by the optically thick dust. In this case, the apparent abundances of N-bearing iCOMs relative to $HCOOCH_3$ would be lower. Even if the dust opacity is not high, the smaller distribution yields a lower beam-averaged column density for the same beam filling factor. According to Csengeri et al. (2019), HCOOH shows a distribution like that of N-bearing iCOMs. Hence, the low abundance of HCOOH relative to $HCOOCH_3$ would also be attributed to its very compact distribution. In the following discussions, we need to keep these caveats in mind.

3.5. Comparison with Chemical Models

Here, we compare the observed molecular abundances with the reported results of chemical network calculations. We first employ the detailed chemical model of hot cores/hot corinos with an emphasis on iCOMs reported by Garrod et al. (2022) for comparison (Table 4). This model is an updated version of that reported by Garrod (2013). In those works, a three-phase model is used, where chemical processes in the gas phase, on the grain surface, and in bulk ice are fully incorporated. Temporal variations of molecular abundances are calculated for the three different warm-up processes, which mimic protostellar birth—namely, the fast, medium, and slow warm-up processes from the cold cloud stage (10 K) to the hot corino stage (100 K). In the model by Garrod et al. (2022), the $HCOOCH_3/CH_3OH$ ratio is 0.02 for the fast warm-up case and becomes slightly higher for slower warm-up cases. The model result is roughly consistent with the range of ratios observed for the hot corino sources including CB 68. The $CH_3OCH_3/HCOOCH_3$ ratio calculated by the model is 0.6–0.9 and does not vary significantly among the three warm-up cases. In the hot corino sources, the ratio is 0.12 −1.9, and hence, the model result fits the observations. The $CH_3CHO/HCOOCH_3$ ratio is 0.21 for the fast warm-up case and slightly increases for slower warm-up cases. It is much higher than the upper limit derived in CB 68, but it is consistent with some hot corinos as shown in Table 3 and Figure 7. The abundance of NH_2CHO calculated in the fast warm-up model is 1/10 of that of $HCOOCH_3$, which is inconsistent with the upper limit measured for CB 68 (<0.006). Note that the calculated $NH_2CHO/HCOOCH_3$ ratio becomes slightly higher for a slower warm-up period in the model. It is still higher than the observed ratio for all of the sources except for NGC 1333 IRAS 2A.

On the other hand, Aikawa et al. (2020) presented chemical network calculations considering the physical evolutions of the static and collapsing phases, where the physical condition was taken from the 1D radiation hydrodynamic model of low-mass star formation presented in Masunaga et al. (1998) and Masunaga & Inutsuka (2000). Their results successfully reproduce both of the chemical features observed in CB 68: (1) the enhancement of carbon-chain molecules and related

Table 3
Abundance Ratios of iCOMs Relative to $HCOOCH_3$

Molecule	CB 68	IRAS 16293[i] Source A	IRAS 16293[ii] Source B	NGC 1333[iii] IRAS 2A	NGC 1333[iv] IRAS 4A2	B335[v]	BHR 71[vi] IRS 1	HH 212[vii]	B1-c[viii]	HOPS-108[ix]	Ser-emb 8[viii]	Ser-emb 11[x]	SVS 13A[xi]
CH_3OCH_3	0.74 ± 0.11	$1.9^{+1.0}_{-0.7}$	$0.9^{+0.3}_{-0.2}$	$0.6^{+0.4}_{-0.3}$	$1.3^{+0.19}_{-0.09}$	$0.73^{+0.12}_{-0.11}$	$0.12^{+0.04}_{-0.03}$	...	$1.26^{+0.09}_{-0.08}$	0.20 ± 0.10	$0.75^{+0.12}_{-0.10}$	$0.69^{+0.08}_{-0.05}$	$0.33^{+0.08}_{-0.07}$
CH_3CHO	<0.07	$0.013^{+0.007}_{-0.005}$	$0.46^{+0.15}_{-0.12}$	...	$0.43^{+0.15}_{-0.14}$	$0.54^{+0.10}_{-0.09}$	...	$0.5^{+0.5}_{-0.2}$	0.24 ± 0.05	0.020 ± 0.004	$0.063^{0.011}_{0.009}$	...	0.08 ± 0.05
NH_2CHO	<0.006	$0.007^{+0.004}_{-0.003}$	0.04 ± 0.02	$0.15^{+0.05}_{-0.06}$	...	$0.092^{+0.014}_{-0.012}$	...	$0.05^{+0.06}_{-0.03}$	0.027 ± 0.013	0.003 ± 0.001	0.017 ± 0.003	$0.0050^{+0.0013}_{-0.0011}$	0.006 ± 0.002
C_2H_5OH	<0.3	$0.30^{+0.15}_{-0.11}$	$0.9^{+0.3}_{-0.2}$	1.0 ± 0.6	...	$0.81^{+0.16}_{-0.14}$	$0.16^{+0.05}_{-0.04}$	$0.8^{+0.9}_{-0.5}$	0.79 ± 0.16	...	$0.19^{+0.03}_{-0.02}$	$0.145^{+0.018}_{-0.013}$	$0.29^{+0.07}_{-0.11}$
C_2H_5CN	<0.02	$0.033^{+0.014}_{-0.008}$	$0.014^{+0.004}_{-0.002}$	$0.019^{+0.006}_{-0.008}$	...	$0.037^{+0.008}_{-0.007}$	...	...	0.057 ± 0.016	$0.006^{+0.004}_{-0.002}$	0.07 ± 0.04	$0.0104^{+0.0019}_{0.0015}$	$0.008^{+0.002}_{-0.003}$
$(CH_3)_2CO$	<0.05	$0.09^{+0.05}_{0.03}$	$0.9^{+0.3}_{-0.2}$	...	$0.15^{+0.03}_{-0.02}$	0.18 ± 0.03	$0.12^{+0.04}_{-0.03}$	...	...	0.055 ± 0.013	$0.35^{+0.05}_{-0.04}$	$0.091^{+0.015}_{-0.012}$	$0.19^{+0.12}_{-0.14}$
HCOOH	<0.03	$0.05^{+0.03}_{-0.02}$	$0.22^{+0.07}_{-0.06}$	...	...	1.0 ± 0.2	...	...	0.037 ± 0.011	...	$0.57^{+0.08}_{-0.06}$	...	0.05 ± 0.02
$L_{bol}/L_{\odot}$	0.86[xii]	21[xiii]	21[xiii]	35.7[xiv]	9.1[xiv]	0.57[xv]	13.5[xvi]	9[vii]	3.2[xvii]	38.3[xviii]	5.4[xix]	4.8[xix]	32.5[xx]
T_{bol}/K	41[xii]	43[xxi]	43[xxi]	50[xiv]	33[xiv]	36[xiv]	51[xvi]	~50[xxii]	46[xvii]	39[xviii]	58[xix]	77[xix]	188[xx]
SED Class	Class 0	Class 0	Class 0	Class 0	Class 0	Class 0	Class 0	Class 0	Class 0	Class 0	Class 0	Class I	Class I

Notes.
[i] Manigand et al. (2020). Calcutt et al. (2018) for C_2H_5CN.
[ii] Jørgensen et al. (2018). Coutens et al. (2016) for NH_2CHO and Calcutt et al. (2018) for C_2H_5CN.
[iii] Taquet et al. (2015).
[iv] López-Sepulcre et al. (2017).
[v] Imai et al. (2016).
[vi] Yang et al. (2020).
[vii] Lee et al. (2019).
[viii] van Gelder et al. (2020) for O-bearing iCOMs and Nazari et al. (2021) for N-bearing iCOMs.
[ix] Chahine et al. (2022).
[x] Martin-Doménech et al. (2021).
[xi] Yang et al. (2021).
[xii] Launhardt et al. (2013).
[xiii] Jørgensen et al. (2016). Source A and Source B are not resolved.
[xiv] Kristensen et al. (2012). A1 and A2 are not resolved.
[xv] Evans et al. (2015).
[xvi] Yang et al. (2018).
[xvii] Karska et al. (2018).
[xviii] Tobin et al. (2019).
[xix] Enoch et al. (2011).
[xx] Tobin et al. (2016).
[xxi] Jørgensen et al. (2002). Source A and Source B are not resolved.
[xxii] Lee et al. (2006). Estimated from T_{dust}.

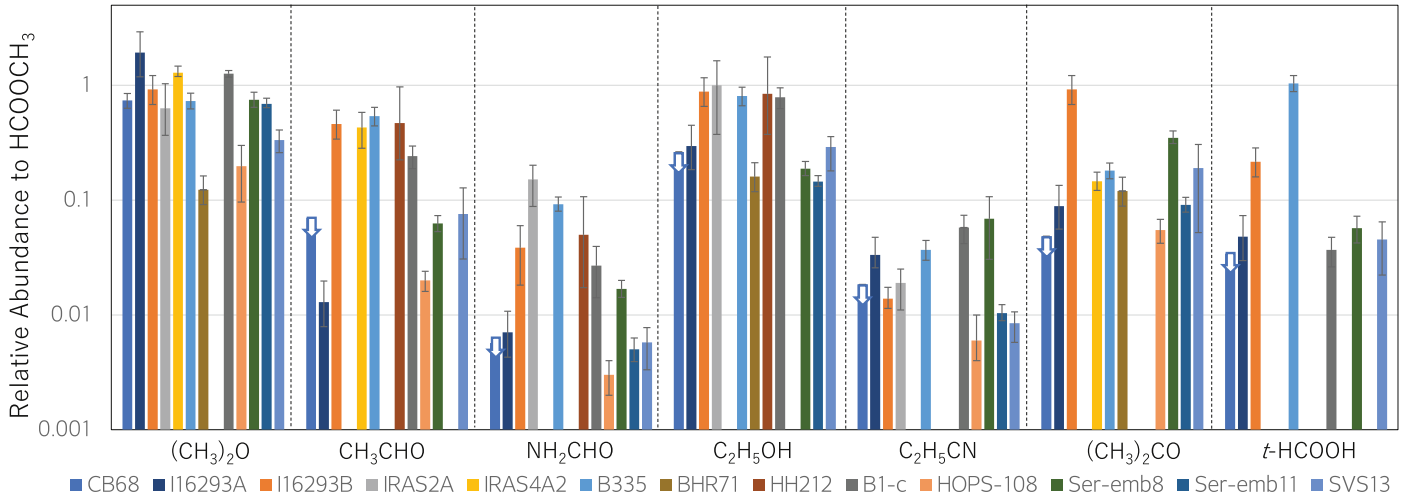

Figure 7. Comparison of relative abundances to $HCOOCH_3$ with several low-mass protostellar sources. Source names are given at the bottom. I16393A denotes IRAS 16293−2422 Source A, I16393B denotes IRAS 16293−2422 Source B, IRAS 2A denotes NGC 1333 IRAS 2A, IRAS 4A2 denotes NGC 1333 IRAS 4A2, and BHR 71 denotes BHR 71 IRS 1. See Table 3 for references.

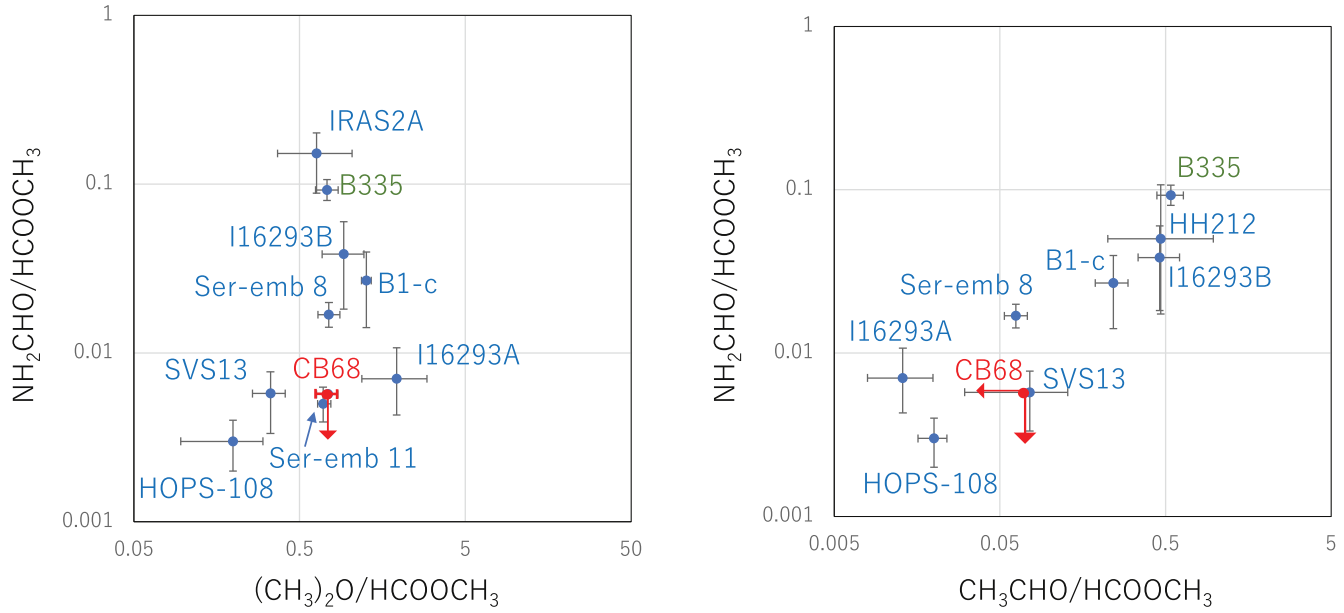

Figure 8. (Left) Plot of the abundances of CH_3OCH_3 and NH_2CHO relative to $HCOOCH_3$. (Right) Plot of the abundances of CH_3OCH_3 and NH_2CHO relative to $HCOOCH_3$.

Table 4
Comparison with Chemical Model[a]

Abundance Ratio	CB 68	Fast[a]	Medium[a]	Slow[a]	Fiducial[b]	T_{min} = 20 K[b]
$CH_3OCH_3/HCOOCH_3$	0.74 ± 0.11	0.58	0.90	0.89	62	1.7
$CH_3CHO/HCOOCH_3$	<0.07	0.21	0.38	1.0	8.4	61
$NH_2CHO/HCOOCH_3$	<0.006	0.10	0.13	0.21	42	290

Notes.
[a] Taken from Garrod (2013). Results for the fast, medium, and slow warm-up cases are shown.
[b] Taken from Aikawa et al. (2020). Results for the fiducial model and the model of the minimum temperature during the static phase of 20 K are listed.

species on a 1000 au scale (i.e., WCCC) and (2) the enrichment of iCOMs in the vicinity of the protostar (i.e., hot corino chemistry). The chemical network is essentially the same as that reported by Garrod (2013) except for some updates of the reactions. However, the details of the ice chemistry model, i.e., a multilayered ice mantle without swapping, are different from those in Garrod (2013), which affects the iCOM abundances.

According to Aikawa et al. (2020), the $HCOOCH_3/CH_3OH$ and $CH_3OCH_3/HCOOCH_3$ abundance ratios in the hot corino stage derived from the chemical network calculation are much

lower and higher, respectively, than the observational results for the hot corino sources including CB 68. Aikawa et al. (2020) also reported that the $CH_3OCH_3/HCOOCH_3$ ratio depends on the lowest temperature T_{min} during the evolution. The ratio changes by two orders of magnitude, where it is close to unity for the case of T_{min} of 20 K: the ratio is higher for lower and higher T_{min} in the range of 10 K to 25 K. For T_{min} of 20 K, the $CH_3OCH_3/HCOOCH_3$ ratio is almost comparable to the observed ratios in hot corinos, while the $CH_3CHO/HCOOCH_3$ and NH_2CHO ratios are significantly overestimated. The $HCOOCH_3$ abundance seems significantly underestimated, and resolving this issue is left for future study.

4. Kinematic Structure

In this section, we explore the kinematic structure of the hot corino and its surrounding envelope. We assume the P.A. of the disk/envelope system to be 232°, perpendicular to the outflow direction (P.A. = 142°) (Wu et al. 1996; Vallée et al. 2000; Launhardt et al. 2010). The disk/envelope direction is shown by dashed lines in Figure 2(a).

Figures 9(a) and (b) show the moment 1 maps of the $C^{18}O$ ($J = 2 - 1$) line and the low-excitation line ($4_{2,3} - 3_{1,2}$ E) of CH_3OH. A velocity gradient along the disk/envelope direction is seen for these two lines, although the gradient in the moment 1 map of $C^{18}O$ looks marginal due to the contribution of the extended component. To investigate the velocity structure in more detail, we draw position–velocity (PV) diagrams along the disk/envelope direction. Figure 9(c) shows the PV diagram of the $C^{18}O$ line along the disk/envelope direction. A diamond-shaped feature can be seen, where the velocity width increases approaching the protostar. Moreover, a marginal velocity gradient, suggesting a rotation motion, is found in the vicinity of the protostar: the southwestern side is redshifted, while the northeastern side is blueshifted. This velocity gradient is more clearly seen in the PV diagram of the low-excitation CH_3OH line observed with the high frequency resolution spectral window (Figure 9(d)). Although the blueshifted emission is rather faint, the velocity gradient is consistent with that found in $C^{18}O$. For further confirmation, we investigate the velocity structure of the OCS ($J = 19 - 18$) emission, which is concentrated around the protostar (Figure 10(a)). Figure 10(b) shows the moment 1 map, while Figure 10(c) depicts the PV diagram along the disk/envelope direction. OCS is also reported to be enhanced in the inner envelope of IRAS 16293−2422 Source A as well as iCOMs (Oya et al. 2016). The velocity gradient ($\sim 0.07\ km\ s^{-1}\ au^{-1}$) is clearly seen in the moment 1 map and the PV diagram of OCS.

The diamond-shaped structure seen in the PV diagram of $C^{18}O$ is a typical feature characteristic of an infalling–rotating envelope (IRE), where the gas is infalling with conserved angular momentum (Ohashi et al. 1997; Oya et al. 2014, 2016; Sakai et al. 2014a). The PV diagram further shows a counter velocity component (blueshifted emission in the southwestern part and redshifted emission in the northeastern part). Such a feature is difficult to explain by a Keplerian motion alone. To compare the kinematic structures of the above molecules, we present a composite PV diagram, where the individual PV diagrams of the $C^{18}O$, CH_3OH, and OCS lines are overlaid in the same panel (Figure 11(a)). Although the distribution of the CH_3OH line is not well resolved, its kinematic structure resembles that of the OCS line. While $C^{18}O$ seems to trace an entire IRE, CH_3OH and OCS most likely trace only the innermost part.

Although the velocity gradient is small, we try to roughly estimate the physical parameters of the IRE. For this purpose, we compare the kinematic structures observed for the $C^{18}O$, CH_3OH, and OCS lines with those derived from a simple model of IREs. Details of the model are described in Oya et al. (2014). This model has successfully been applied to the IREs of some low-mass protostellar sources (e.g., Sakai et al. 2014a; Oya et al. 2015; Oya et al. 2016; Oya et al. 2017; Imai et al. 2019; Oya & Yamamoto 2020). In this model, the structure of the IRE is determined by six free parameters: the kinematic structure is specified by (1) the radius of the centrifugal barrier (r_{CB}) and (2) the mass of the central protostar (M_*), while the shape of the IRE is specified by (3) the outer radius of the emitting region in the envelope (R_0), (4) the full thickness of the envelope (h_0), (5) the flare angle of the envelope, and (6) the inclination angle (i) with respect to the line of sight ($i = 90°$ for the edge-on case).

In the CB 68 model, we make the following assumptions. The outer radius is fixed to 600 au by referring to the distribution of the $C^{18}O$ emission. We assume the inclination angle to be 70° (nearly edge-on disk). This assumption seems reasonable because the well-collimated outflow feature (Vallée et al. 2000) suggests a nearly edge-on geometry of the disk. Moreover, the fitting results do not depend on inclination angles ranging from 50° to 90°, although the protostellar mass is correlated with them ($\propto \sin^{-2} i$). We arbitrarily assume a flare angle of the envelope of 10° and that the full thickness of the envelope is 100 au. We confirm that the results do not significantly change for a flare angle between 0° and 30° and for a thickness between 10 au and 100 au. This is because the resolution of the present observation ($\sim 0\farcs4-0\farcs5$; 70−80 au) is insufficient to place strong constraints on these parameters.

Figure 11(b) shows the result of the model calculation overlaid on the composite PV diagram. The velocity structure including the counter velocity component seems to be reproduced with r_{CB} of 3 au and M_* of 0.15 $M_\odot$. We use these values as the fiducial values to find the acceptable ranges of the parameters. To estimate the ranges of r_{CB} and M_*, we change their values from the above fiducial ones and compare the results with the composite PV diagram by eye. Figure 12 shows a comparison with the composite PV diagram. In the comparison, we focus on the overall velocity extent rather than the detailed intensity distribution because the latter is difficult to reproduce quantitatively due to various factors such as the self-absorption effect and the inhomogeneous distribution not considered in the IRE model. The velocity shift is mainly affected by M_* because the velocity of the gas at a certain radius is roughly proportional to $M_*^{1/2}$ in the IRE model. Considering that the OCS and CH_3OH emission has higher velocity components than the $C^{18}O$ emission around the protostar position, we conservatively adopt the range of 0.08 $M_\odot$ to 0.30 $M_\odot$ for M_*. On the other hand, r_{CB} affects the velocity gradient in the PV diagram. The observed PV diagrams can be reasonably explained by r_{CB} less than 30 au for the models assuming M_* of 0.15 $M_\odot$. This result is not changed if M_* is changed in the above range. For instance, the case for 0.3 $M_\odot$ is shown in Figure 12 (bottom panel).

5. Comparison with B335

In this section, we discuss the similarities and differences between CB 68 and B335, both of which are isolated Class 0

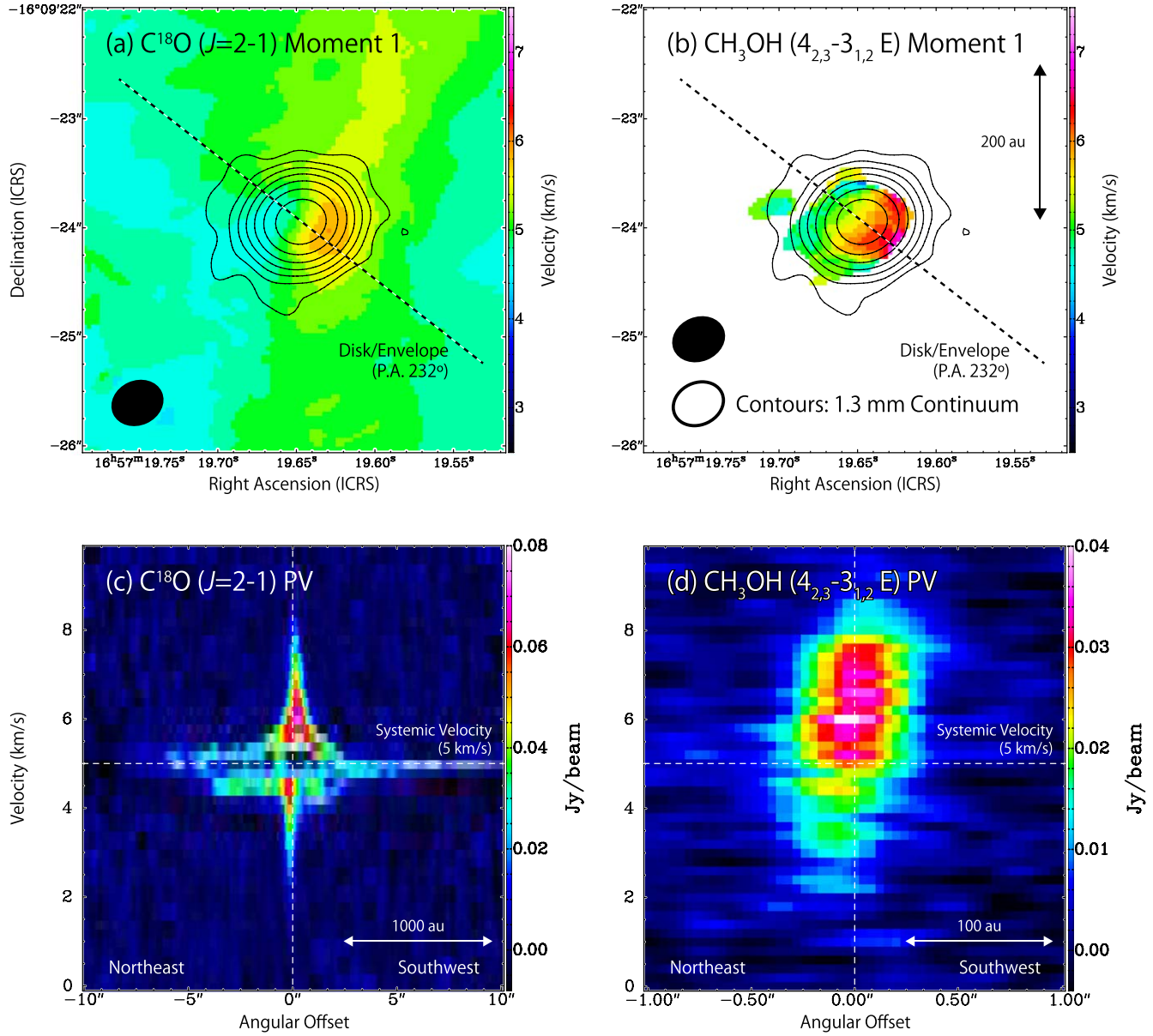

Figure 9. (a), (b) The velocity field maps (moment 1 maps) of $C^{18}O$ and CH_3OH. Black filled ellipses represent the beam sizes. Cube data with intensities less than 3σ are not used. Furthermore, positions with integrated intensities less than 3σ are shown in white. Contours represent the continuum image of Figure 1, and a black open ellipse shows its beam size. Dashed lines represent the disk/envelope direction, along which the PV diagrams are presented. (c) The PV diagram of $C^{18}O$ along the disk/envelope direction shown in Figure 2. (d) The PV diagram of CH_3OH along the disk/envelope direction. A smaller range of the position offset is employed to see the velocity gradient clearly.

protostellar sources in Bok globules and have similar bolometric luminosities and bolometric temperatures (Table 3). Note that BHR 71 IRS 1 is also a Class 0 protostar in a Bok globule, whose chemical composition may be compared with that of CB 68 in the context of isolated protostars. However, this source accompanies another protostar IRS 2 separated from IRS 1 by 16″, and hence, it is not in a fully isolated condition like CB 68 and B335. Furthermore, the abundances are obtained for a limited species, and data on NH_2CHO and CH_3CHO, which show relatively low abundances in CB 68, are not available (Yang et al. 2020). For these reasons, we do not particularly discuss BHR 71 IRS 1 for detailed comparison with CB 68 in this paper.

The protostellar mass of CB 68 estimated in this study is likely higher than the mass of B335 ($0.02-0.06\,M_{\odot}$; Imai et al. 2019). Only the upper limit to the radius of the centrifugal barrier is obtained for both sources (<5 au for B335 and <30 au for CB 68). These radii are smaller than those previously reported for the other protostellar sources L1527 (100 ± 20 au; Sakai et al. 2014b), IRAS 16293−2422 Source A (40−60 au; Oya et al. 2016), and TMC-1A (~50 au; Sakai et al. 2016). The comparatively small centrifugal barrier indicates a relatively small specific angular momentum of the accreting gas and that infalling motion is dominant in the protostellar envelope. Hence, the Keplerian disk has not grown to a sufficient size to be detected inside the centrifugal barrier. Although we cannot resolve structures finer than 30 au in this study, a small emitting region of CH_3OH indicates that the size of the hot corino is about 10 au. If iCOMs are distributed in the transition zone from the envelope to the disk as reported for IRAS 16293−2422 Source A

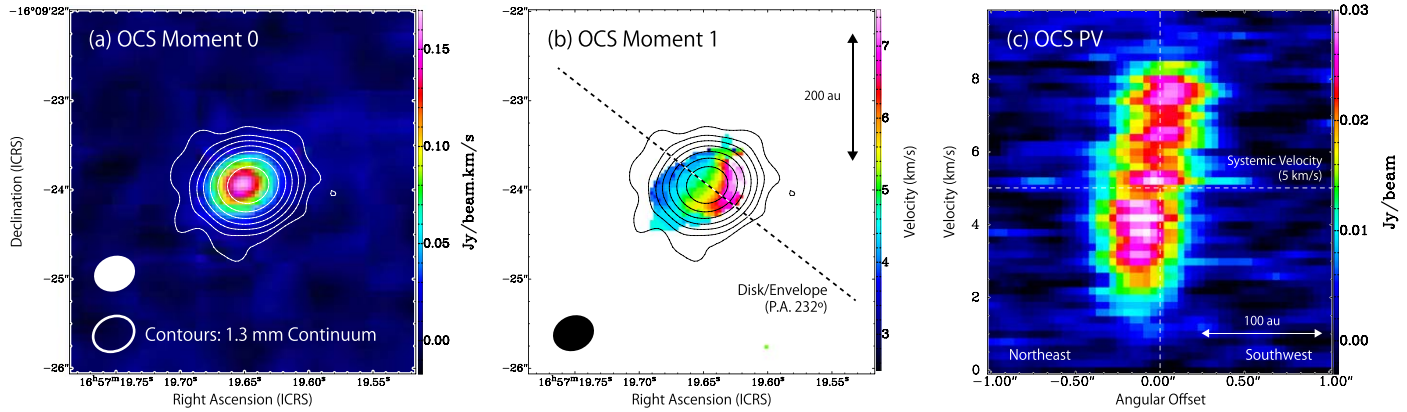

Figure 10. The integrated intensity map (left), the moment 1 map (middle), and the PV diagram of OCS along the disk/envelope direction (right), where a dashed line in the middle panel shows the disk/envelope direction. The velocity range for the integrated intensity map is 0.0 km s^{-1} to 9.8 km s^{-1}. Contours on the left and middle panels represent the continuum emission (Figure 1). See the caption of Figure 9 for the preparation of the moment 1 map. The rms noise level of the integrated intensity map is 4 mJy beam^{-1} km s^{-1}. On the left panel, a white filled ellipse represents the beam size of the OCS image, while a white open ellipse represents that of the 1.3 mm continuum image. On the middle panel, a black filled ellipse represents the beam size of the OCS image. A velocity gradient is visible in the moment 1 map and the PV map.

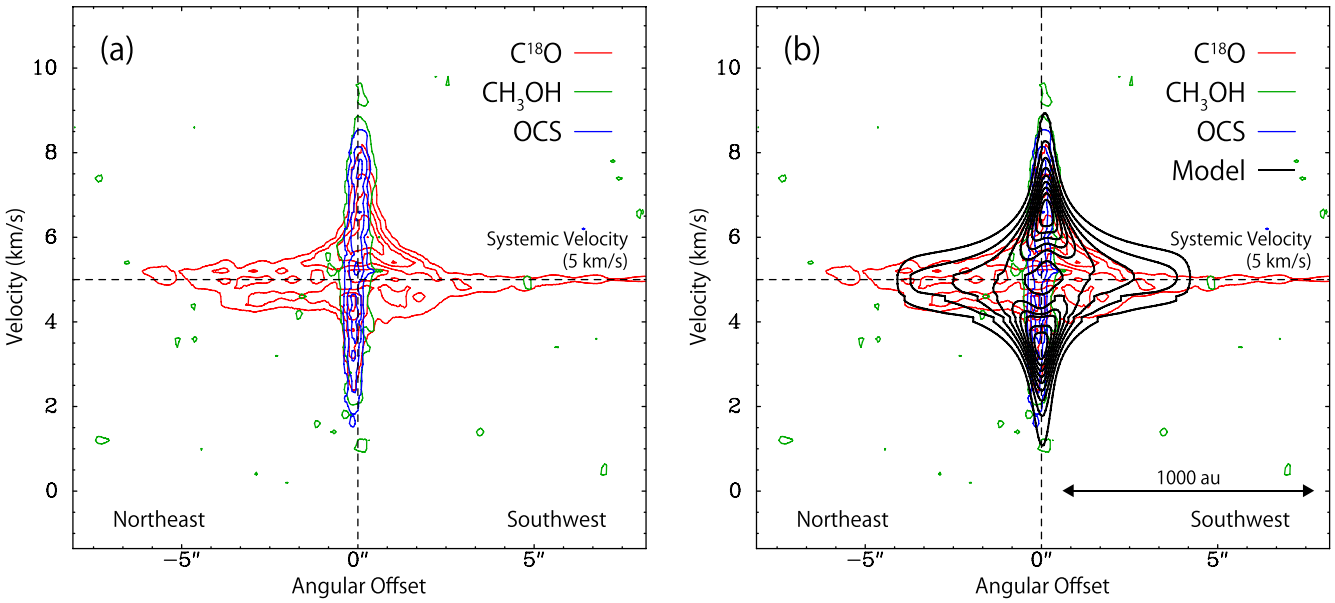

Figure 11. (a) A composite PV diagram of $C^{18}O$ (red), CH_3OH (green), and OCS (blue), which represents the kinematic structure for a wide spatial range. (b) Same as (a) but with the result of the IRE model using the fiducial values of the model parameters (black contours). See Section 4 for details. The position shows the offset from the continuum peak.

and B335 (Oya et al. 2016; Imai et al. 2019), the small emitting region of CH_3OH is consistent with the small radius of the centrifugal barrier. In this case, a weak accretion shock would be responsible for the liberation of iCOMs around the centrifugal barrier (Sakai et al. 2014b; Oya et al. 2016; Garufi et al. 2022). Although the disk size of Class 0 protostellar sources is reported to be generally small (Maury et al. 2019), the very small radius for CB 68 and B335 might be related to their isolated condition. For instance, it is suggested that higher exposure to the interstellar radiation field can increase the local ionization fraction, which would produce small disk structures (e.g., Zhao et al. 2018; Kueffmeier et al. 2020). However, we should note that this suggestion is still controversial (Zhao et al. 2020).

Given the physical conditions detailed above, we find that the overall chemical structure of CB 68 resembles that of B335. CB 68 is a hybrid type consisting of a WCCC on the 1000 au scale and a hot corino chemistry on the scale of a few tens of astronomical units around the protostar. Such a feature is consistent with the result of the chemical network calculation by Aikawa et al. (2020), as mentioned in Section 3.5. This result seems consistent with the idea that the parent cores of isolated sources like CB 68 and B335 are well exposed to the interstellar radiation field, which may prevent the total conversion of C into CO and subsequent iCOM formation on dust grains. On the other hand, unsaturated hydrocarbons are produced efficiently in the gas phase. In a small central part where the extinction is large enough, C-to-CO conversion efficiently occurs, as does iCOM formation on dust grains.

Although the isolated sources CB 68 and B335 both show a hybrid chemical nature, we should note that a hybrid chemical nature is not specific to isolated sources. Indeed, a hybrid chemistry is reported for L483 (Oya et al. 2017), and a hint of it is also seen in Serpens SMM 3 (Tychoniec et al. 2021).

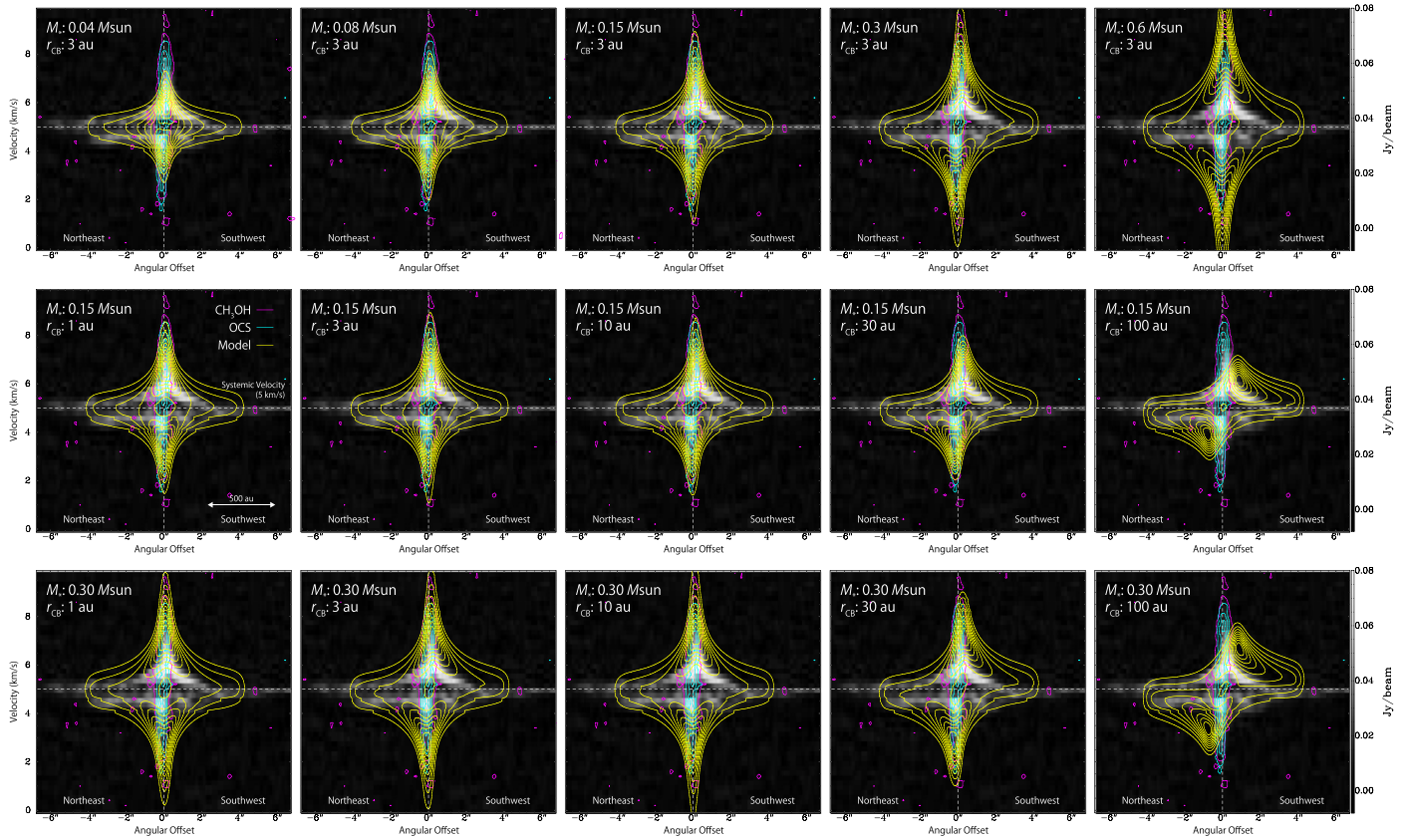

Figure 12. Results of the IRE model with various parameters (yellow contours) superposed on the composite PV diagram shown in Figure 11(a). $C^{18}O$ is presented in gray scales, CH_3OH in magenta, and OCS in cyan. The position shows the offset from the continuum peak. The protostellar mass of 0.08−0.30 $M_\odot$ and the radius of the centrifugal barrier (r_{CB}) of 30 au or less can reasonably reproduce the observed kinematic structure.

Nevertheless, the simple physical and chemical structures of isolated sources can be used as the best testbed to study chemical evolution during protostellar evolution without the influence of nearby young stellar objects.

Despite such great similarity between CB 68 and B335, there is one notable relative chemical difference between the two sources—namely, CH_3CHO, NH_2CHO, and HCOOH are less abundant in CB 68 than in B335 (Table 3). This difference remains unexplained. Although it could be ascribed to the different local densities/temperatures, we have yet to consider the effect of the dust opacity in the iCOM-emitting region before further investigating the chemistry. The FAUST project will further explore other protostellar sources at 50 au resolution with equivalent sensitivity and will provide the additional observations necessary to address this problem.

6. Summary

Observations of CB 68 at the 1.3 mm band were conducted with ALMA to characterize the chemical and physical structures of the protostellar envelope. The main results are summarized below.

1. Carbon-chain-related molecules CCH and c-C_3H_2 as well as $C^{18}O$ are detected in the envelope on a scale of 1000 au. The overall distribution of the c-C_3H_2 emission is concentrated around the continuum peak, indicating the WCCC nature of the source. The CCH emission seems to trace the outflow cavity extending to the northwestern direction, as well.
2. CH_3OH, CH_2DOH, $HCOOCH_3$, and CH_3OCH_3 are detected in the vicinity of the protostar on a scale less than the beam size (∼70–80 au). The detection of iCOMs clearly indicates that CB 68 harbors a hot corino. The rotation temperature of CH_3OH is derived to be 131 ± 11 K by assuming an LTE condition. The emitting region of CH_3OH is as small as 10 au.
3. The $HCOOCH_3/CH_3OH$ and $CH_3OCH_3/HCOOCH_3$ ratios obtained in this source are comparable to those in other hot corino sources and B335. On the other hand, CH_3CHO, NH_2CHO, and HCOOH are less abundant than in other sources.
4. Hybrid-type chemical characteristics (hot corino chemistry and WCCC) are thus revealed in CB 68, which resemble the case of another isolated protostellar source B335.
5. The whole envelope structure is traced by $C^{18}O$, while only the innermost part of the envelope is traced by CH_3OH and OCS. These molecules show a marginal velocity gradient perpendicular to the outflow (disk/envelope direction). The PV diagram along the disk/envelope direction is explained by the IRE model. The protostellar mass and the radius of the centrifugal barrier are estimated to be 0.08–0.30 $M_\odot$ and <30 au, respectively. The small centrifugal barrier may be related to the small emitting region of iCOMs, if the iCOM emission mainly originates from the transition zone around the centrifugal barrier.

The authors thank the anonymous reviewer for valuable comments and suggestions. This paper makes use of the

following ALMA data: ADS/JAO.ALMA#2016.1.01376.S. ALMA is a partnership of ESO (representing its member states), NSF (USA) and NINS (Japan), together with NRC (Canada), NSC and ASIAA (Taiwan), and KASI (Republic of Korea), in cooperation with the Republic of Chile. The Joint ALMA Observatory is operated by ESO, AUI/NRAO and NAOJ. The authors acknowledge financial support from JSPS and MAEE under the Japan–France Integrated Action Program (SAKURA: 25765VC). D.J. is supported by NRC Canada and by an NSERC Discovery Grant. E.B. and G.B. acknowledge funding from the European Research Council under the European Union's Horizon 2020 research and innovation program, for the project "The Dawn of Organic Chemistry," grant agreement No. 741002. G.B. acknowledges support from the PID2020-117710GB-I00 grant funded by MCIN/AEI/10.13039/501100011033 and from the Unit of Excellence María de Maeztu 2020–2023 award to the Institute of Cosmos Sciences (CEX2019-00918-M). I.J.-S. has received partial support from the Spanish State Research Agency (AEI) through project Nos. PID2019-105552RB-C41 and MDM-2017-0737 Unidad de Excelencia "Maria de Maeztu" - Centro de Astrobiologia (CSIC-INTA). This study is supported by grants-in-aid from the Ministry of Education, Culture, Sports, Science, and Technology of Japan (18H05222, 18J11010, 19H05069, 19K14753, and 21K13954).

ORCID iDs

Muneaki Imai https://orcid.org/0000-0002-5342-6262
Yoko Oya https://orcid.org/0000-0002-0197-8751
Brian Svoboda https://orcid.org/0000-0002-8502-6431
Bertrand Lefloch https://orcid.org/0000-0002-9397-3826
Serena Viti https://orcid.org/0000-0001-8504-8844
Yichen Zhang https://orcid.org/0000-0001-7511-0034
Cecilia Ceccarelli https://orcid.org/0000-0001-9664-6292
Claudio Codella https://orcid.org/0000-0003-1514-3074
Claire J. Chandler https://orcid.org/0000-0002-7570-5596
Nami Sakai https://orcid.org/0000-0002-3297-4497
Yuri Aikawa https://orcid.org/0000-0003-3283-6884
Felipe O. Alves https://orcid.org/0000-0002-7945-064X
Nadia Balucani https://orcid.org/0000-0001-5121-5683
Eleonora Bianchi https://orcid.org/0000-0001-9249-7082
Mathilde Bouvier https://orcid.org/0000-0003-0167-0746
Gemma Busquet https://orcid.org/0000-0002-2189-6278
Paola Caselli https://orcid.org/0000-0003-1481-7911
Emmanuel Caux https://orcid.org/0000-0002-4463-6663
Steven Charnley https://orcid.org/0000-0001-6752-5109
Spandan Choudhury https://orcid.org/0000-0002-7497-2713
Nicolas Cuello https://orcid.org/0000-0003-3713-8073
Marta De Simone https://orcid.org/0000-0001-5659-0140
Francois Dulieu https://orcid.org/0000-0001-6981-0421
Cécile Favre https://orcid.org/0000-0002-5789-6931
Siyi Feng https://orcid.org/0000-0002-4707-8409
Francesco Fontani https://orcid.org/0000-0003-0348-3418
Logan Francis https://orcid.org/0000-0001-8822-6327
Tetsuya Hama https://orcid.org/0000-0002-4991-4044
Tomoyuki Hanawa https://orcid.org/0000-0002-7538-581X
Eric Herbst https://orcid.org/0000-0002-4649-2536
Shingo Hirano https://orcid.org/0000-0002-4317-767X
Tomoya Hirota https://orcid.org/0000-0003-1659-095X
Andrea Isella https://orcid.org/0000-0001-8061-2207
Izaskun Jímenez-Serra https://orcid.org/0000-0003-4493-8714
Doug Johnstone https://orcid.org/0000-0002-6773-459X
Claudine Kahane https://orcid.org/0000-0003-1691-4686
Romane Le Gal https://orcid.org/0000-0003-1837-3772
Laurent Loinard https://orcid.org/0000-0002-5635-3345
Ana López-Sepulcre https://orcid.org/0000-0002-6729-3640
Luke T. Maud https://orcid.org/0000-0002-7675-3565
María José Maureira https://orcid.org/0000-0002-7026-8163
Francois Menard https://orcid.org/0000-0002-1637-7393
Anna Miotello https://orcid.org/0000-0002-7997-2528
George Moellenbrock https://orcid.org/0000-0002-3296-8134
Shoji Mori https://orcid.org/0000-0002-7002-939X
Riouhei Nakatani https://orcid.org/0000-0002-1803-0203
Hideko Nomura https://orcid.org/0000-0002-7058-7682
Yasuhiro Oba https://orcid.org/0000-0002-6852-3604
Ross O'Donoghue https://orcid.org/0000-0002-5317-6304
Satoshi Ohashi https://orcid.org/0000-0002-9661-7958
Yuki Okoda https://orcid.org/0000-0003-3655-5270
Jaime Pineda https://orcid.org/0000-0002-3972-1978
Linda Podio https://orcid.org/0000-0003-2733-5372
Albert Rimola https://orcid.org/0000-0002-9637-4554
Takeshi Sakai https://orcid.org/0000-0003-4521-7492
Dominique Segura-Cox https://orcid.org/0000-0003-3172-6763
Vianney Taquet https://orcid.org/0000-0003-0407-7489
Leonardo Testi https://orcid.org/0000-0003-1859-3070
Naoki Watanabe https://orcid.org/0000-0001-8408-2872
Yoshimasa Watanabe https://orcid.org/0000-0002-9668-3592
Ci Xue https://orcid.org/0000-0003-2760-2119
Satoshi Yamamoto https://orcid.org/0000-0002-9865-0970

References

Aikawa, Y., Furuya, K., Yamamoto, S., et al. 2020, ApJ, 897, 110
Aikawa, Y., Wakelam, V., Garrod, R. T., & Herbst, E. 2008, ApJ, 674, 984
Ambrose, H. E., Shirley, Y. L., & Scibelli, S. 2021, MNRAS, 501, 347
Bertrang, G., Wolf, S., & Das, H. S. 2014, A&A, 565, A94
Bianchi, E., Chandler, C. J., Ceccarelli, C., et al. 2020, MNRAS, 498, L87
Bjerkeli, P., Ramsey, J. P., Harsono, D., et al. 2019, A&A, 631, A64
Calcutt, H., Jørgensen, J. K., Müller, H. S. P., et al. 2018, A&A, 616, A90
Caselli, P., & Ceccarelli, C. 2012, A&ARv, 20, 56
Cazaux, S., Tielens, A. G. G. M., Ceccarelli, C., et al. 2003, ApJL, 593, L151
Chahine, L., López-Sepulcre, A., Neri, R., et al. 2022, A&A, 657, A78
Chini, R. 1981, A&A, 99, 346
Codella, C., Ceccarelli, C., Chandler, C., et al. 2021, FrASS, 8, 782006
Coutens, A., Jørgensen, J. K., van der Wiel, M. H. D., et al. 2016, A&A, 590, L6
Csengeri, T., Belloche, A., Bontemps, S., et al. 2019, A&A, 632, A57
Endres, C. P., Schlemmer, S., Schilke, P., et al. 2016, J. Mol. Spectrosc., 337, 95
Enoch, M. L., Corder, S., Duchene, G., et al. 2011, ApJS, 195, 21
Evans, N. J., II, Di Francesco, J., Lee, J.-E., et al. 2015, ApJ, 814, 22
Feng, S., Beuther, H., Henning, Th., et al. 2015, A&A, 581, A71
Frerking, M. A., Langer, W. D., & Wilson, R. W. 1982, ApJ, 262, 590
Garrod, R. T. 2013, ApJ, 765, 60
Garrod, R. T., Jin, M., Matis, K. A., et al. 2022, ApJS, 259, 1
Garufi, A., Podio, L., Codella, C., et al. 2022, A&A, 658, A104
Herbst, E., & van Dishoeck, E.F. 2009, ARA&A, 47, 427
Higuchi, A. E., Sakai, N., Watanabe, Y., et al. 2018, ApJS, 236, 52
Imai, M., Oya, Y., Sakai, N., et al. 2019, ApJL, 873, L21
Imai, M., Sakai, N., Oya, Y., et al. 2016, ApJL, 830, L37
Jiménez-Serra, I., Zhang, Q., Viti, S., et al. 2012, ApJ, 753, 34
Jørgensen, J. K., Müller, H. S. P., Calcutt, H., et al. 2018, A&A, 620, A170
Jørgensen, J. K., Schöier, F. L., & van Dishoeck, E. F. 2002, A&A, 389, 908
Jørgensen, J. K., van der Wiel, M. H. D., Coutens, A., et al. 2016, A&A, 595, A117

Karska, A., Kaufman, M. J., Kristensen, L. E., et al. 2018, ApJS, 235, 30
Kristensen, L. E., van Dishoeck, E. F., Bergin, E. A., et al. 2012, A&A, 542, A8
Kueffmeier, M., Zhao, B., & Caselli, P. 2020, A&A, 639, A86
Launhardt, R., Evans, N. J., II, Wang, Y., et al. 1998, ApJS, 119, 59
Launhardt, R., & Henning, T. 1997, A&A, 326, 329
Launhardt, R., Nutter, D., Ward-Thompson, D., et al. 2010, ApJS, 188, 139
Launhardt, R., Stutz, A. M., Schmiedeke, A., et al. 2013, A&A, 551, A98
Lee, C.-F., Codella, C., Li, Z.-Y., et al. 2019, ApJ, 876, 63
Lee, C.-F., Ho, P. T. P., Beuther, H., et al. 2006, ApJ, 639, 292
Lemme, C., Wilson, T. L., Tieftrunk, A. R., et al. 1996, A&A, 312, 585
Lindberg, J. E., Jørgensen, J. K., Watanabe, Y., et al. 2015, A&A, 584, A28
Lombardi, M., Lada, C. J., & Alves, J. 2008, A&A, 480, 785
López-Sepulcre, A., Sakai, N., Neri, R., et al. 2017, A&A, 606, A121
Mainzer, A., Bauer, J., Cutri, R. M., et al. 2014, ApJ, 792, 30
Manigand, S., Jørgensen, J. K., Calcutt, H., et al. 2020, A&A, 635, A48
Martin-Doménech, R., Bergner, J. B., Öberg, K. I., et al. 2021, ApJ, 923, 155
Masunaga, H., & Inutsuka, S. 2000, ApJ, 531, 350
Masunaga, H., Miyama, S. M., & Inutsuka, S. 1998, ApJ, 495, 346
Maury, A. J., André, Ph., Testi, L., et al. 2019, A&A, 621, A76
McMullin, J. P., Waters, B., Schiebel, D., Young, W., & Golap, K. 2007, in ASP Conf. Ser. 376, Astronomical Data Analysis Software and Systems XVI, ed. R. A. Shaw, F. Hill, & D. J. Bell (San Francisco, CA: ASP), 127
Nazari, P., van Gelder, M. L., van Dishoeck, E. F., et al. 2021, A&A, 650, A150
Nozawa, S., Mizuno, A., Teshima, Y., et al. 1991, ApJS, 77, 647
Ohashi, N., Hayashi, M., Ho, P. T. P., & Momose, M. 1997, ApJ, 475, 211
Ohashi, S., Codella, C., Sakai, N., et al. 2022, ApJ, 927, 54
Okoda, Y., Oya, Y., Abe, S., et al. 2021b, ApJ, 923, 168
Okoda, Y., Oya, Y., Francis, L., et al. 2021a, ApJ, 910, 11
Ortiz-Leon, G. N., Loinard, L., Kounkel, M. A., et al. 2017, ApJ, 834, 141
Oya, Y., López-Sepulcre, A., Sakai, N., et al. 2019, ApJ, 881, 112
Oya, Y., Moriwaki, K., Onishi, S., et al. 2018a, ApJ, 854, 96
Oya, Y., Sakai, N., Lefloch, B., et al. 2015, ApJ, 812, 59
Oya, Y., Sakai, N., López-Sepulcre, A., et al. 2016, ApJ, 824, 88
Oya, Y., Sakai, N., Sakai, T., et al. 2014, ApJ, 795, 152
Oya, Y., Sakai, N., Watanabe, Y., et al. 2017, ApJ, 837, 174
Oya, Y., Sakai, N., Watanabe, Y., et al. 2018b, ApJ, 863, 72
Oya, Y., & Yamamoto, S. 2020, ApJ, 904, 185
Park, W., Lee, J.-E., Contreras, P. C., et al. 2021, ApJ, 920, 132
Pickett, H. M., Poynter, R. L., Cohen, E. A., et al. 1998, JQSRT, 60, 883
Sakai, N., Oya, N., López-Sepulcre, A., et al. 2016, ApJL, 820, L34
Sakai, N., Oya, Y., Sakai, T., et al. 2014a, ApJL, 791, L38
Sakai, N., Sakai, T., Hirota, T., et al. 2008, ApJ, 672, 371
Sakai, N., Sakai, T., Hirota, T., et al. 2010, ApJ, 722, 1633
Sakai, N., Sakai, T., Hirota, T., et al. 2014b, Natur, 507, 78
Sakai, N., & Yamamoto, S. 2013, ChRv, 113, 8981
Spezzano, S., Bizzocchi, L., Caselli, P., Harju, J., & Brünken, S. 2016, A&A, 592, L11
Taquet, V., López-Sepulcre, A., Ceccarelli, C., et al. 2015, ApJ, 804, 81
Tobin, J. J., Looney, L. W., Li, Z.-Y., et al. 2016, ApJ, 818, 73
Tobin, J. J., Thomas Megeath, S., van't Hoff, M., et al. 2019, ApJ, 886, 6
Tychoniec, L., van Dishoeck, E. F., van't Hoff, M. L. R., et al. 2021, A&A, 655, A65
Vallée, J. P., Bastien, P., & Greaves, J. S. 2000, ApJ, 542, 352
van Gelder, M. L., Tabone, B., Tychoniec, L., et al. 2020, A&A, 639, A87
Wu, Y., Huang, M., & He, J. 1996, A&AS, 115, 283
Yamamoto, S. 2017, Introduction to Astrochemistry: Chemical Evolution from Interstellar Clouds to Star and Planet Formation (Berlin: Springer)
Yang, Y.-L., Evans, N. J., II, Smith, A., et al. 2020, ApJ, 891, 61
Yang, Y.-L., Green, J. D., Evans, N. J., II, et al. 2018, ApJ, 860, 174
Yang, Y.-L., Sakai, N., Zhang, Y., et al. 2021, ApJ, 910, 20
Zhang, Y., Higuchi, A. E., Sakai, N., et al. 2018, ApJ, 864, 76
Zhao, B., Caselli, P., Li, Z.-Y., & Krasnopolsky, R. 2018, MNRAS, 473, 4868
Zhao, B., Tomida, K., Hennebelle, P., et al. 2020, SSRv, 216, 43
Zucker, C., Speagle, J. S., Schlafly, E. F., et al. 2019, ApJ, 879, 125